SURFACE SIGNATURE OF FLOW PAST A SPHERE AT MODERATE REYNOLDS NUMBERS

A Thesis

by

QI SHAO

Submitted to the Office of Graduate and Professional Studies of
Texas A&M University
in partial fulfillment of the requirements for the degree of

MASTER OF SCIENCE

Chair of Committee,	Robert Handler
Committee Members,	Je-Chin Han
	Helen Reed
Head of Department,	Andreas Polycarpou

May 2014

Major Subject: Mechanical Engineering

ABSTRACT

The incompressible viscous flow past a sphere is investigated numerically at moderate Reynolds numbers. Periodic vortex shedding happens at these Reynolds numbers. The primary objective is to identify the surface signature when the wake reaches the surface. The numerical method is a direct numerical simulation based on finite volume method using open-sourced code OpenFOAM. This work can contribute to the detection of underwater obstacles.

The unsteady flow is calculated at Reynolds number of 300. The flow shows a planar symmetric pattern with vortex shedding. When Reynolds number increases to 500, the flow becomes more chaotic and loses its planar symmetry. At Reynolds number of 500, highly organized periodic surface signatures appear on the shear-free surface when the sphere is near the surface. The signatures are identified as the cold regions with hot edges when constant heat flux is performed on the surface. There is a pair of vortices with opposite rotating directions inside the signature, which can be visualized by passive Lagrangian particles. The incompressible flow acts like compressible flow on the surface because the surface divergence and convergence happen.

At Reynolds number of 500, the cylindrical vortex sheet is reorganized into vortex rings due to complex instabilities effects. The periodic vortex rings attach the surface to form the periodic thermal surface signatures.

DEDICATION

To my God,

To my parents,

for love.

ACKNOWLEDGEMENTS

First I would like to thank my advisor, Dr. Robert Handler. He has always been a true mentor and friend in every day I worked with him. He is not only a knowledgeable teacher, but also a good listener. We had delightful discussions for research problems that we faced. I learned much from his guidance and patience.

I also would like to thank the members of my committee, Dr. Je-Chin Han and Dr. Helen Reed. They provided many good advices to make a better thesis for me. Thanks also go to my friends and colleagues Qi Zhang, Youfeng Zhang and Gustavo Rojas. They provided valuable help for me and we had a great experience working together.

Finally, thanks to my mother, father and all my families. For me, nothing can replace their love.

NOMENCLATURE

2D	Two-dimensional
3D	Three-dimensional
p	Pressure
T	Temperature
U	Velocity
T	Time
g	Gravitational acceleration
k	Thermal conductivity
ν	Kinematic viscosity
μ	Dynamic viscosity
ρ	Density
d	Diameter
r	Radius
f	Frequency
α	Thermal diffusivity
c_p	Specific heat
F_d	Drag force
C_d	Drag coefficient
Pr	Prandtl number
St	Strouhal number

Re	Reynolds number
Fr	Froude number
We	Weber number
σ	Surface tension
q	Eddy velocity
L	Eddy length scale

TABLE OF CONTENTS

Page

LIST OF FIGURES

FIGURE Page

LIST OF TABLES

TABLE Page

1. INTRODUCTION AND LITERATURE REVIEW

1.1 Objective

This research can contribute to the detection of non-acoustic signatures of underwater objects, such as submarines. Sometimes submarines will move close to the surface of ocean. They will generate turbulent wake behind them when moving. The wake will attach the surface to form some pattern of surface signature. Understanding the formation of the surface signature can help develop the technology to detect it.

Compared to the previous theoretical investigation of Milgram and experimental investigation of Walker, a direct numerical simulation (DNS) is performed in this work to simulate the flow field of underwater objects.

1.2 Background

1.2.1 Turbulent wake

A turbulent wake is produced when fluid flows past an underwater object at moderate speeds. The nature of these was depends on many factors such as the flow speed and the geometry of the object. If the object is sufficiently close to the surface of ocean or river, the wake will spread and interact with the surface and generate phenomena like surface roughness, wave motion and surface temperature change. These phenomena are still poorly understood because of the complexity of turbulent wake itself and the interactions between it and the free surface.

1.2.2 Thermal signature

Infrared (IR) sensors can respond to the hydrodynamic effects generated by underwater objects on the ocean surface. When an underwater object moves several body diameters beneath the ocean surface, there are three primary hydrodynamic signatures:

a. A change of the surface flow velocity when wake interacts with the ambient surface current.

b. Deformation of ocean surface in the form of propagating waves or non-wave deformation.

c. Thermal signature due to two environmental effects, namely the cool-skin/warm-skin effects and effects related to oceanic thermal stratification (Peltzer [23]).

Paulson and Simpson [21] reported that the surface of ocean is often found to be colder than the water just a few millimeters below. It usually takes place at night when radiation is primary responsible for surface cooling, and also takes place during the day as a result of wind driven forced convection. A warm-skin effect may occur in some conditions during daylight hours if solar heating dominates over cooling on the ocean surface. In both cases, a thin thermal boundary layer exists with a temperature difference around one half to one degree centigrade depending on the ocean surface heat flux. Thermal signatures can also be found because of oceanic thermal stratification (Pedlosky [22]) related to temperature difference between the ocean surface and he fluid at depth, which is typically 2 to 3 degrees centigrade. Therefore, the wake of an underwater object can produce a thermal signature on the ocean surface by transporting the fluid from

below to the surface. Thus a visible thermal ‘scar’ will be generated because of the temperature difference between the ambient ocean surface and the subsurface fluid which has been transported to the surface.

Figure 1 was an IR image taken from an aircraft over the Potomac River approximately 60 km south of Washington, DC. This image was obtained by Dr. Geoffrey Smith of the Naval Research Laboratory. The intensity represents temperature while darker shades mean lower temperature. The red lines are bathymetry with the innermost circle about 1.8 m, and about 1.8 m between lines. The dark scars at the upper left and lower right portions of the image are old boat wakes. The dark lines crossing the wakes are data anomalies and should be ignored. The maximum temperature difference in the image is about 1 degree centigrade. This image proves the feasibility of detection of the thermal signature.

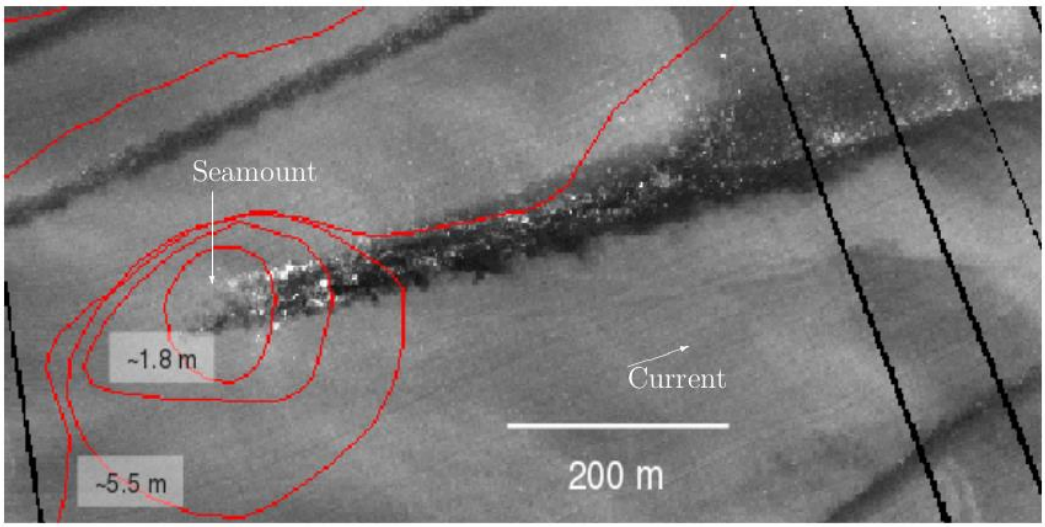

Figure 1. Thermal scar of a non-breaching seamount at the bottom of the Potomac River.

1.2.3 Surface deformation

There are three dimensionless parameter related to the physical process: The Reynolds number (Re), Froude number (Fr) and Weber number (We). Following Brocchini and Peregrine, they are defined as $Re = UD/\nu$, $Fr = q/\sqrt{2gL}$, and $We = [(\rho q^2/2)L/\sigma]$.

Here L is defined as the size of a typical turbulent 'eddy' (e.g. its radius). q is a typical turbulent velocity 'fluctuation' associated to the eddy. g is the gravitational acceleration. ρ is the fluid density. ν is the kinematic viscosity. σ is the surface tension. D is the length scale characterizing the object (diameter for a sphere). U is the average flow velocity.

Here we study the case of water, the fluid density and surface tension will be fixed. Given a fixed velocity U an object size D, Re will be fixed. Then we discuss the free surface deformation in the Fr – We space. We can express the turbulent eddy velocity q as $q = Fr\sqrt{2gL}$ and $q = We^{1/2}\sqrt{2\sigma/\rho L}$, thus defining a q – L space in place of a Fr – We space. This gives the more easily visualized physical parameters q and L in place of Fr and We. Brocchini and Peregrine [6] developed an approximate way to determine the region in which the free surface will break apart to become a two-phase (air and water) flow. This flow represents the most severe disruption of the free surface, not the situation in which the surface is merely deformed or remains smooth an nearly affected by subsurface turbulence. Using the vortex ring as a rough model for a typical turbulent eddy, the dividing line between complete surface breakup and mind surface deformation can be obtained. The kinetic energy of a 'thin' ring whose radius R is much

larger than its core diameter is of the order of $\rho\gamma^2 R/2$ (Batcholor [2]), where γ refers to the circulation around the ring. If all the kinetic energy of the ring is converted to the potential energy of a droplet that remains stationary at the free surface as shown in Figure 2, we have:

$$\frac{\rho\gamma^2 R}{2} = \rho\left(\frac{4}{3}\pi R^3\right)gR + 4\pi R^2\sigma \tag{1.1}$$

With the circulation $\gamma \approx 2\pi Rq$, the relation between q and L is obtained

$$q^2 = \frac{2}{3\pi}Rg + \frac{2}{\pi}\frac{\sigma}{\rho R} \tag{1.2}$$

The other relations,

$$q = Fr^*\sqrt{2gL} \tag{1.3}$$

$$q = (We^*)^{1/2}\sqrt{\frac{2\sigma}{\rho L}} \tag{1.4}$$

With $Fr^* = 1/\sqrt{3\pi}$ and $We^* = 1/\pi$ represent cases in which surface tension force and gravity are negligible respectively.

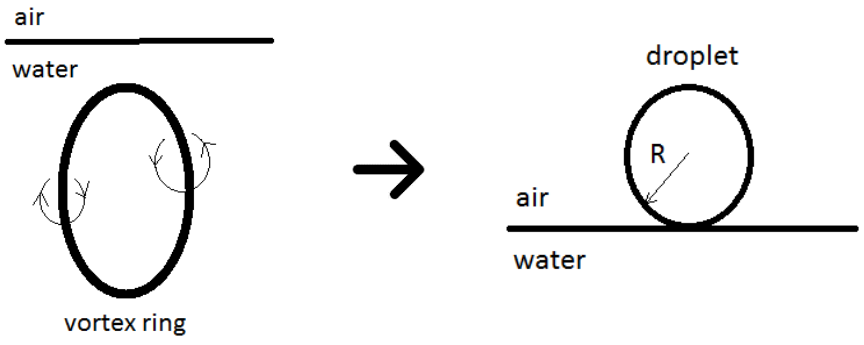

Figure 2. The conversion from a vortex ring to a droplet.

The three curves given by equations 2, 3 and 4 are plotted in Figure 3. The curves of equations 3 and 4 divide q – L space into four regions with special physical significance. In general, the turbulent flow must overcome the restoring forces of gravity and surface tension for subsurface turbulent eddies to cause significant surface deformation.

Region 1: Both Fr and We are small. Gravity and surface tension are strong enough to suppress surface deformation effectively. Weak deformation such as dimples formed by attached subsurface vortices (Bernal and Kwon [4]) may exist. But generally the free surface will be smooth and glass-like, despite the subsurface turbulence.

Region 2: Gravitational force is not strong enough to keep the surface flat, while surface tension force is relatively strong. It results in small scale surface deformation such as capillary waves and small scale microbreakers (Melville, [16]).

Region 3: Neither gravity nor surface tension are strong enough to suppress surface deformation. It results in the surface breaking into droplets, bubbles, and sprays so that the air-water interface must be considered as a two-phase flow.

Region 4: Gravitational force tends to suppress the surface deformation, while the surface tension force is weak. It results in the gravity waves and regions of deformation related to convergent and divergent lows which are commonly refer to as scars. In this case, complex gravity waves are generated with “scars” at the edge of the wake which can persist for a very long distance.

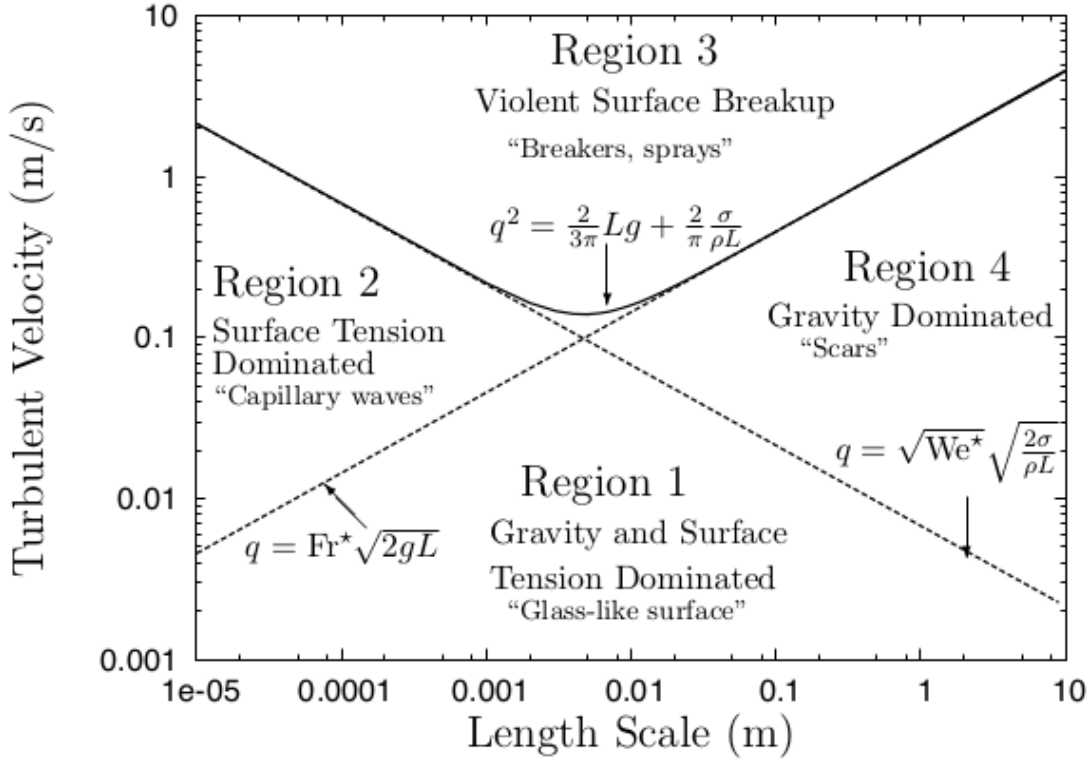

Figure 3. Regimes of turbulence generated free-surface deformation.

In this work, water flow past a sphere at Reynolds number of 500 is studied. In this case, the water inlet velocity v = 0.01m/s, sphere diameter D = 0.05m. We assume eddy length scale L = D = 0.05m, eddy velocity q = 0.2v=0.002m/s.

At L = 0.05m, $q = Fr^*\sqrt{2gL} = 0.32m/s \gg 0.002m/s$ for equation 3 and $q = (We^*)^{\frac{1}{2}}\sqrt{\frac{2\sigma}{\rho L}} = 0.03m/s \gg 0.002m/s$ for equation 4. So this point is in region 1. Hence in this case the surface deformation is very weak and the surface will be very flat.

1.2.4 Existing technology

Crocker [3] pointed out the rapid development of ultra-quiet diesel-electric (DE) and air-independent propulsion (AIP) submarines whose hull and plant noise signatures fell below the signal-to-noise levels detectable by the Navy's passive detection systems, especially in noisy littoral areas.

As far back as 1966, the Office of Naval Research researched into the use of infrared lasers to detect surface anomalies, including the Bernoulli Hump (a surface bulge of displaced water left by shallow-running submarines) and Kelvin Waves (the characteristic V-shaped wakes left by objects moving through the water). In a series of US patents beginning in 1971, explored practical systems were invented to employ blue-green lasers. Let's look briefly at some of the technologies:

US 3,604,803 (1971 – Kahn): The '803 Patent describes an airborne system that uses a broad and narrow beam pulsing laser to look for the "shadow" caused by a submarine in the path of the beams.

US 4,867,558 (1989 – Leonard, et al – subsequently assigned to GTE Government Systems): The '558 Patent's abstract describes an airborne system that uses pulsed beams to read thermoclines.

US 4,893,924 (1990 – Leonard, et al – assigned to GTE Government Systems): The '924 Patent – filed by the same inventor group – describes a submarine-based system:

US 7,283,426. (2007 – Grasso – assigned to BAE Systems): The ’426 Patent describes an airborne pulse laser to sense water particle movement within a water column shot with the laser.

1.3 Flow regimes at different Reynolds numbers

Jones and Clarke [12] noted that the nature of the flow around a sphere changes dramatically as the Reynolds number of the flow increases. In general, the higher the Reynolds number, the more complex the flow is. In this section the nature of the flow for different Reynolds numbers is described. It should be noticed that the Reynolds number range for each of the different flow regimes may be different depending on the individual researchers.

1.3.1 Steady axisymmetric without separation regime: Re < 25

There is a theoretical solution for flow past a sphere at sufficiently low Reynolds numbers ($\mathrm{Re} \ll 1$), which is called the Stokes flow. In this case, the flow field is perfectly symmetric. Lamb [14] included detailed solutions for Stokes flow in his book *Hydrodynamics*.

Taneda [29] and Nakamura [18] performed experimental investigations of the steady wake behind a sphere at low Reynolds numbers. Taneda [29] found that for Reynolds numbers less than 24 the flow around the sphere is perfectly laminar. There is no flow separation. In this case, the flow on the downstream side of the sphere is nearly identical to that on the upstream side. Magarvey and Bishop [15] noted that the

streamlines followed the interface and exhibited symmetry for the sphere for small Reynolds numbers.

1.3.2 Steady axisymmetric with separation regime: 25 < Re < 210

When Reynolds number of about 25 is reached, a small permanent separation area appears in the neighborhood of the rear stagnation point. As the Reynolds number increases, it grows and becomes more and more elongated in the flow direction. Taneda [29] showed that the size of the separation area was nearly proportional to the logarithm of the Reynolds number. After Reynolds number of approximately 130, oscillations began to appear at the rear of the separation area with a very long period. However Nakamura [18] found that the separation area was stable up to a Reynolds number of 190. Magarvey & Bishop [15] found the same behavior occurring up to Re = 210. These observations are in good agreement with the numerical results of Tomboulides [32] from a spectral element solution of flow over a sphere. He found the transition to steady flow at Re=212. Natarajan and Acrivos [19] found a regular bifurcation at *Re*=210 using finite-element method. And they suggest that this corresponds to the transition from the steady axisymmetric wake to the steady, non-axisymmetric, double-thread wake.

1.3.3 Steady planar symmetric regime: 210 < Re < 270

Magarvey & Bishop [15] and Wu & Faeth [33] noted that the flow remained stable but was no longer axisymmetric above approximately Re = 210. The axisymmetry is replaced by a planar symmetry. The flow in this regime consists of two streamwise

vortical tails of equal strength and opposite sign. Magarvey and Bishop [5] referred to this structure as a double threaded wake.

The orientation of the symmetry plane is tilted off the streamwise axis. Johnson and Patel [11] explained this by the azimuthal instability of the low pressure core of the wake vortex. Actually the orientation of the plane is arbitrary and is determined by random external influences, such as perturbations due to model supports in an experimental situation, or truncation errors or grid asymmetries in numerical simulations.

The loss of axial symmetry leads to the appearance of a lateral (lift) force, which is directed in the plane of flow symmetry. The presence of this force was found by Magarvey and Bishop [15] by noticing that the liquid drops in their experiments deviated from a vertical line of fall. The lateral force has been verified by several numerical simulations. Gushchin [8] found zero lift force at Re = 210 but a finite value at Re = 210.5 using an explicit second order finite difference scheme to perform direct numerical simulations. Johnson and Patel [11] found that between Re = 211 and Re = 212 the simulated lift force jumped by three orders of magnitude.

Tomboulides and Orszag [31] performed direct numerical simulation based on a mixed spectral element/Fourier spectral method to simulate the flow between Re = 25 and Re =1000. They showed that the flow is axisymmetric up to a Reynolds number of approximately 212. Beyond this Reynolds number, the flow undergoes a transition to three-dimensionality through a regular bifurcation. The flow is stable up to a Reynolds number of approximately 270, corresponded to the double-thread wake reported in the experiment of Magarvey and Bishop [15]. The double-thread wake consists of two

infinite opposite-sign streamwise vortices and appears in the experiment as two dye threads emanating from the end of the recirculation region. It is also characterized by a loss of axisymmetry in the path of falling sphere (Magarvey and Bishop [15]).

1.3.4 Unsteady planar symmetric regime: 270 < Re < 400

The steady planar symmetric wake turns to a time-dependent planar-symmetric periodic wake as the Reynolds number increases. The unsteadiness first appears as a waviness in the double threaded wake between Re = 270 and Re = 290 reported by Magarvey and Bishop [15]. They found the trail assumes a repetitive pattern and the circulation within the sheet ceases to resemble a symmetrical vortex ring above Re = 290. Wu and Faeth [33] found that the recirculation zone was no longer stable and vortex shedding began at a Reynolds number close to 280.

Numerical simulations also got similar results. Johnson and Patel [11] performed numerical simulations for Re up to 300. They found that a no-axisysmmeric solution at Re = 270 and a clearly periodic solution at Re = 280. The results of their simulation at Re = 300 showed a highly organized periodic flow with vortex shedding, with a Strouhal number of 0.137 and a mean value for the drag coefficient C_d of 0.656. Ploumhans [25] used three-dimensional vortex methods to simulate the flow past a sphere at Reynolds numbers of 300, 500 and 1000. At Re = 300 the flow attained a time periodic regime with a Strouhal number of 0.135 and an average value for C_d of 0.683.

Tomboulides and Orszag [31] showed that the transition leads to a time-dependent solution occurs between Re = 270 and Re = 285 in direct numerical

simulation. Their solution at Re = 300 has the Strouhal number of 0.136 and a mean drag coefficient of 0.671. They noted that the basic wake structure consisted of a succession of interconnected vortex loops which, for low Reynolds numbers, are shed with the same orientation from the sphere; this results in planar symmetry which is observed in the flow up to a Reynolds number between 350 and 450.

1.3.5 Unsteady asymmetric regime: 400 < Re < 800

The planar symmetry of the flow is lost in this range because the azimuthal location at which the vortex loops are formed changes in an irregular fashion. It is difficult to specify the exact value of the Reynolds number at which this begins to happen. The experiments of Sakamoto and Haniu [28] showed that the vortex shedding started to become irregular near Re = 420 and was completely random at Re = 480. Mittal [17] found that the wake began to lose planar symmetry between Re = 350 and Re = 375, and a complete loss of planar symmetry Re = 425. However the planar symmetry still exists at Re=400 in the simulation of Dallmann [7].

At Re = 500, the direct numerical simulations of Tomboulides and Orszag [31] showed a similar wake structure to the one at Re = 300, but the vortex loops were shed from the sphere with different orientations. Hence the planar symmetry was not preserved. The power spectrum of the velocity showed that the flow had changed from a one-frequency flow at Re = 300 to an almost chaotic system at Re = 500 with a dominant peak at a Strouhal number of 0.167.

Near Re = 800, a further transition in the nature of the flow occurs. The measurements of Kim and Durbin [13] showed that two dominant modes of unsteadiness exist in the wake above this Reynolds number. They are associated with small scale instability in the separating shear layer (the Kelvin-Helmhotz instability) and a large scale instability in the wake (the vortex shedding). The higher frequency component could only be detected in the region immediately downstream of the sphere, which led Kim and Durbin to the explanation that this mode correspond to the Kelvin-Helmholtz instability in the separating shear layer. The Strouhal number related with vortex shedding was found to be approximately 0.2 independent of Reynolds number. But the Strouhal number related with the Kelvin-Helmholtz instability increased with Reynolds number. Sakamoto and Haniu [28] found similar results in the experiment. Tomboulides and Orszag [31] also found the presence of a Kelvin-Helmholtz instability in the cylindrical shear layer above Re = 800 in their numerical simulation, which resulted in small scales in the flow.

1.3.6 Turbulent wake regime: Re > 800

In this turbulent regime, the flow can be divided into two regimes, the subcritical regime (800< Re < 370,000, and the supercritical regime (Re >370, 000).

In the subcritical regime, the drag coefficient decreases. It is associated with the transition of the thin viscous boundary layer from laminar to turbulent at the surface of the sphere. Known as the “drag crisis”, this drop in drag coefficient is a direct result of the transition from a laminar boundary layer to a fully turbulent boundary layer, which

causes the attached point moving past the sphere's "top". The frequency associated with the large scale vortices shedding from the sphere is at $St = fD/U \approx 0.2$, where f is the shedding frequency and St is the Strouhal number. The Strouhal number is found to be independent to Reynolds number. Due to Kelvin-Helmholtz mechanism, the instability of the shear layer produced by the separation of boundary layer generates another higher Reynolds number dependent frequency.

Above the critical Reynolds number around Re = 3.7×10^5, the near-wake recirculation region considerably shrinks, the drag coefficient sharply decreases to a value of $C_d \approx 0.08$, and periodic vortex shedding is no longer able to be detected experimentally. Taneda [30] showed experimentally that the wake formed a pair of streamwise line vortices at a short distance from the streamwise axis, and the vortex pair rotated slowly and randomly around that axis in the range $3.8 \times 10^5 < \text{Re} < 1 \times 10^6$.

A summary of flow regimes different Reynolds numbers is contained in Table 1.

Table 1. Flow regimes at different Reynolds numbers

	Nature of Flow	Drag coefficient	Strouhal number	Flow visualization
$Re \leq 25$	Steady axisymmetric flow without recirculation	C_d decreases from very large number to about 2.4	Steady state flow	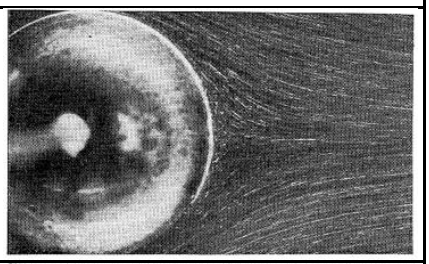
$25 \leq Re \leq 210$	Steady axisymmetric flow with closed recirculation	$2.4 \rightarrow 0.7$	Steady state flow	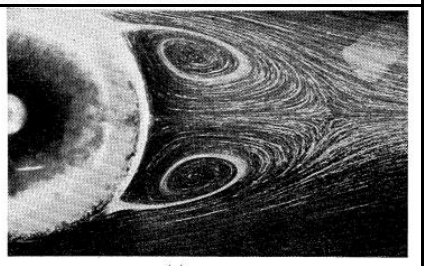
$210 \leq Re \leq 270$	Flow is steady and planar symmetric, consists of two infinite streamwise vortical tails of equal strength and opposite sign.	C_d literally decreases	Steady state flow	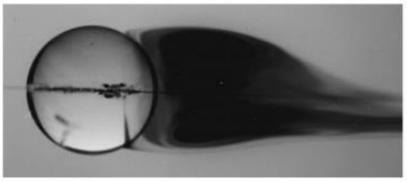 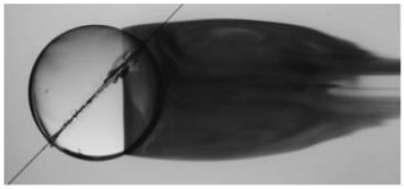
$270 \leq Re \leq 290$	Transition to unsteady. Flow is unsteady and planar symmetric.	Mean value of $C_d \approx 0.66 - 0.68$	$St \approx 0.13 - 0.14$	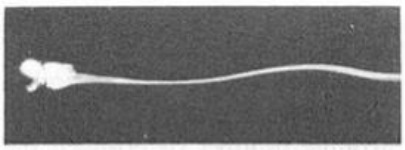
$290 \leq Re \leq 400$	Flow is unsteady and planar symmetric, consisting of periodic shedding of vortex loops.	C_d literally decreases	St increases	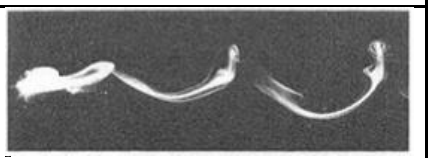 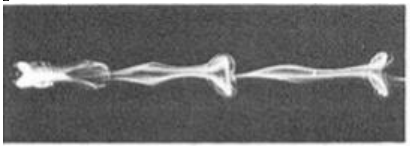

Table 1 Continued

	Nature of Flow	Drag coefficient	Strouhal number	Flow visualization
$400 \leq Re \leq 800$	Vortex loops continue to be shed and the planar symmetry is lost. Flow begins to be chaotic.	Mean value falls to 0.5 at Re = 800	St slowly increases to 0.2 at Re = 800	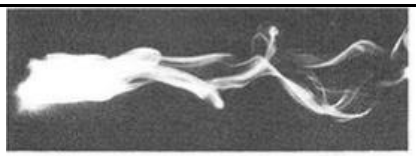
$800 \leq Re \leq 370,000$	Vortex loops continue to be shed but in a more turbulent manner, though strong periodic fluctuations still exist in the wake.	$C_d \approx 0.5$ over entire range	$St \approx 0.2$ over entire range	

2. NUMERICAL METHOD

2.1 The governing equations of fluid dynamics

The water flow can be regarded as incompressible Newtonian flow. We assume density ρ is a constant.

The governing equations for incompressible flow are：

Conservation of mass

$$\nabla \cdot \boldsymbol{v} = 0 \tag{2.1}$$

Conservation of linear momentum

$$\frac{\partial \boldsymbol{v}}{\partial t} + (\boldsymbol{v} \cdot \nabla)\boldsymbol{v} = -\frac{\nabla p}{\rho} + \nu \nabla^2 \boldsymbol{v} \tag{2.2}$$

Thermal energy equation

$$\frac{\partial T}{\partial t} + (\boldsymbol{v} \cdot \nabla)\boldsymbol{v} = \nu \nabla^2 T \tag{2.3}$$

The temperature is considered as a passive scalar in all the simulations of this work. Hence the buoyancy effect is neglected.

The first two equations for Newtonian fluids are normally referred to the Navier-Stokes equations, which is a non-linear set of differential equations that describes the flow of a fluid whose stress depends linearly on velocity gradients and pressure. The unsimplified equations do not have a general closed-form solution, so they are primarily of use in Computational Fluid Dynamics (CFD).

2.2 Numerical method

2.2.1 Finite volume discretization

OpenFOAM uses the Finite Volume method (FVM) for the discretization of Navier-Stokes equation. The Finite Volume method of discretization has the following properties:

a. It is based on the discretization of the integral form of governing equations over each control volume. Therefore, the basic quantities will be conserved at the discrete level, such as mass and momentum.

b. The Equations are solved in a fixed Cartesian coordinate system on the time-fixed mesh. For both steady-state and transient calculations, this method is applicable.

c. The control volumes can be a general polyhedral shape with a variable number of neighbors. Thus an arbitrarily unstructured mesh is created. The control volumes are shared by all dependent variables. It is usually called the collocated or non-staggered variable arrangement (Rhie and Chow [26], Peric [24]).

2.2.2 Algorithm

The solver used in this simulation is icoFoam, which is based on PISO Algorithm for transient incompressible flow.

The PISO procedure proposed by Issa [9] is used for pressure-velocity coupling in transient calculations. For steady-state calculations, a SIMPLE pressure-velocity coupling procedure by Patankar [20] is used.

The pressure-velocity treatment for transient flow calculations was originally proposed by Issa [9] and Jasak [10] summarized the PISO algorithm in the following:

There are three stages of this algorithm: momentum predictor, pressure solution and explicit velocity correction.

Momentum predictor: The momentum equation is solved first. At this stage, the exact pressure gradient source term is not known. So the pressure field from the previous time-step is used instead. The solution of the momentum equation gives an approximation of the new velocity field.

Pressure solution: The pressure equation can be formulated using the predicted velocities. The solution of the pressure equation provides the first estimate of the new pressure field.

Explicit velocity correction: The face flux provides a set of conservative fluxes consistent with the new pressure field. The velocity field need be corrected as a consequence of the new pressure distribution as well. And velocity correction is performed in an explicit manner.

2.2.3 Solution procedure for the Navier-Stokes system

Jasak [10] described the solution sequence for the Navier-Stokes system with additional coupled transport equations (e.g. a turbulence model, energy equation or some

other equations that influence the system). Jasak [10] summarized the transient solution procedure for incompressible turbulent flows as follows:

a. Set up initial conditions for all field values.

b. Start the calculation of the values at new time steps.

c. Solve the momentum predictor equation with the available face fluxes.

d. Stay in the PISO loop until the tolerance of pressure-velocity system is reached. At this stage, pressure/velocity fields and the new set of conservative fluxes for the current time-step are obtained.

e. Solve all other equations in the system using the conservative fluxes. Calculate the effective viscosity from the turbulence variables if turbulence occurs.

f. Return to step b if the final time is not reached.

2.3 Boundary conditions

The domain in the simulation is a cuboid with a sphere in side. So the boundaries include inlet, outlet, top, bottom, front, back and sphere surface in Figure 4. The boundary conditions for all the boundaries are in the Table 2.

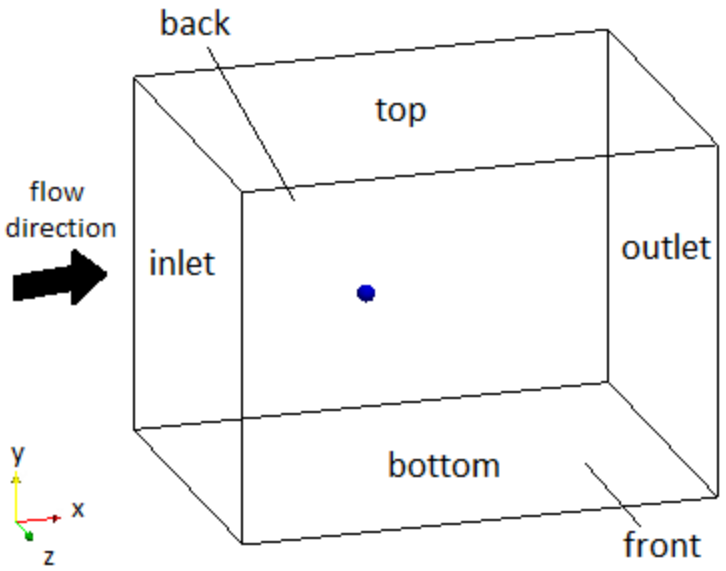

Figure 4. Boundaries of the computational domain.

Table 2. Boundary conditions

	velocity	pressure	temperature
inlet	*u=constant, v=w=0*	$\frac{\partial p}{\partial x} = 0$	*T=constant*
outlet	$\frac{\partial u}{\partial x} = 0, \frac{\partial v}{\partial x} = 0, \frac{\partial w}{\partial x} = 0$	*p=constant*	$\frac{\partial T}{\partial x} = 0$
top	$\frac{\partial u}{\partial y} = 0, v = 0, \frac{\partial w}{\partial y} = 0$	$\frac{\partial p}{\partial y} = 0$	$\frac{\partial T}{\partial y} = constant$
bottom	$\frac{\partial u}{\partial y} = 0, v = 0, \frac{\partial w}{\partial y} = 0$	$\frac{\partial p}{\partial y} = 0$	$\frac{\partial T}{\partial y} = 0$
front	$\frac{\partial u}{\partial z} = 0, \frac{\partial v}{\partial z} = 0, w = 0$	$\frac{\partial p}{\partial z} = 0$	$\frac{\partial T}{\partial z} = 0$
back	$\frac{\partial u}{\partial z} = 0, \frac{\partial v}{\partial z} = 0, w = 0$	$\frac{\partial p}{\partial z} = 0$	$\frac{\partial T}{\partial z} = 0$
sphere surface	*u=v=w=0*	*Normal gradient of p is 0*	*Normal gradient of T is 0*

3. NUMERICAL RESULTS

3.1 Numerical results at Reynolds number of 300

A direct numerical simulation is performed for flow past a sphere at Re=300.

3.1.1 Simulation parameters

As shown in Figure 5, the size of the computational domain is 28D (where D is the diameter of the sphere) in the length, 21D in the width and height. The sphere center is 10.5D from the inlet and in the center with respect to the width and height. There are approximately 1.3 million cells in the mesh. Figure 6 shows the mesh in the cross-section plane from the side and the mesh near the sphere.

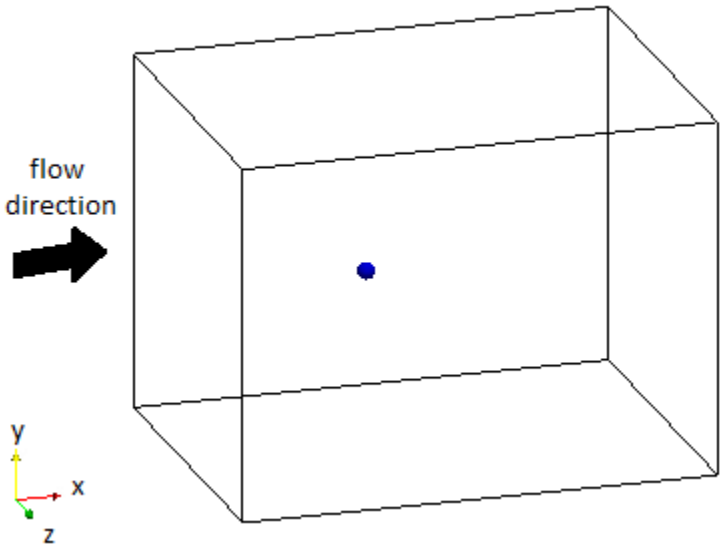

Figure 5. Domain of numerical simulation

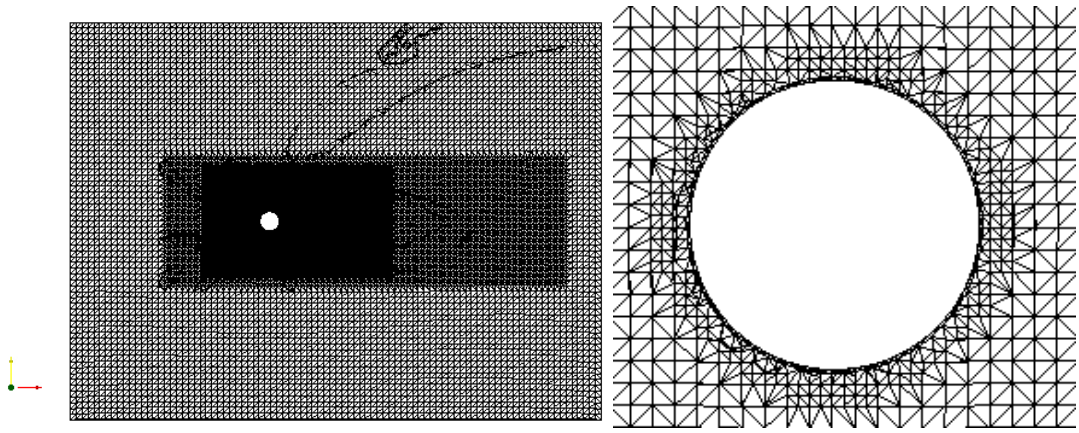

Figure 6. (a) The mesh from the side (b) The mesh near the sphere

For numerical scheme, fourth order is performed in space, second order in time.

In order to trigger the flow into periodic state, random noise is added at the inlet, the magnitude is 2% of the inlet velocity. After the flow become periodic, the noise is turned off. And the periodic shedding of the flow can remain from then on.

3.1.2 Flow pattern

For flow past a sphere at Re=300, the periodic vortex shedding happens. The basic wake structure consists of a succession of interconnected vortex loops, as observed in visualization experiments like those of Magarvey & Bishop [15] and Johnson & Patel [11]. This is in agreement with the velocity magnitude field in the simulation performed by OpenFOAM in Figure 7.

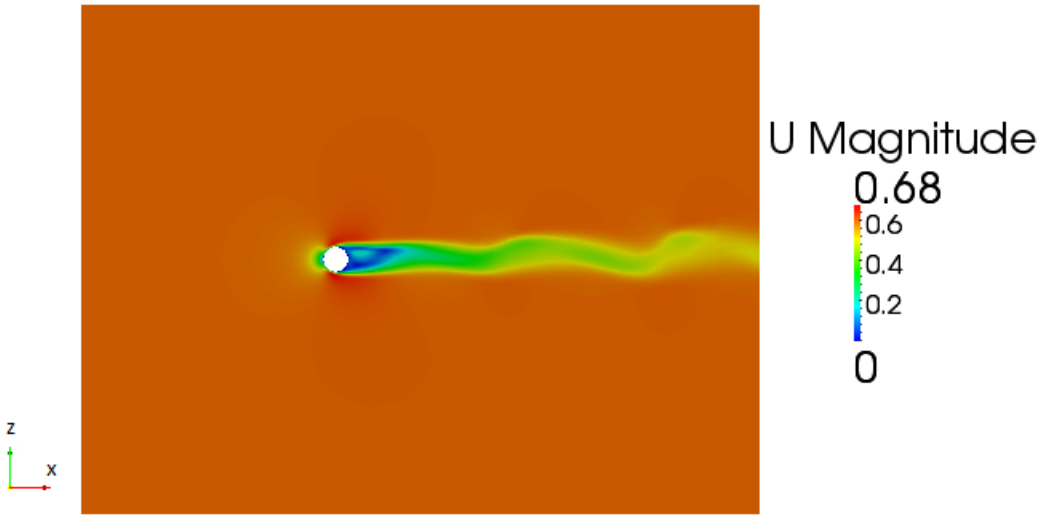

Figure 7. Side view of velocity magnitude at one instant of time of Re = 300.

To visualize the vortex shedding process, isosurfaces of streamwise vorticity are plotted in Figure 8, which show that the vortex loops are always shed from the sphere with the same orientation. The wake maintains planar symmetric.

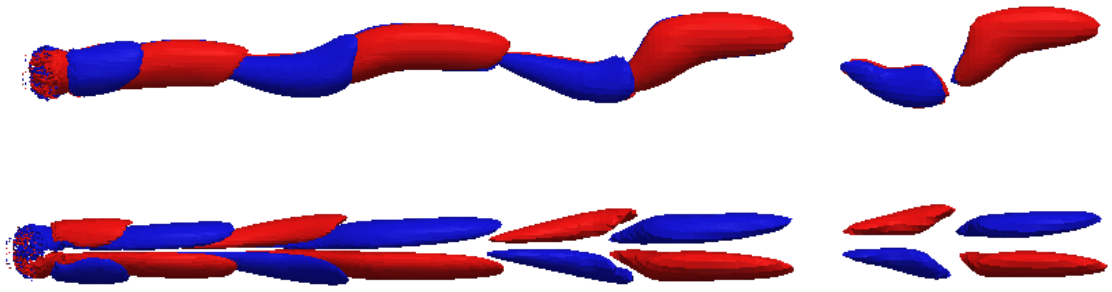

Figure 8. Isosurfaces of streamwise vorticity at one instant of time of Re = 300.

3.1.3 Drag coefficient and Strouhal number

In fluid dynamics, the drag coefficient (C_d) is a dimensionless quantity that is used to quantify the drag or resistance of an object in a fluid environment such as air or water.

The drag coefficient C_d is defined as:

$$C_d = \frac{F_d}{\rho U^2 A} \tag{3.1}$$

Where A is the reference area, for a sphere, $A = \pi r^2$.

In dimensional analysis, the Strouhal number (St) is a dimensionless number describing oscillating flow mechanisms. The Strouhal number is often given as $St = fl/U$, where f is the frequency of vortex shedding, l is the characteristic length (in this case the characteristic length is the diameter of the sphere l = d) and U is the velocity of the fluid.

The result of the drag coefficient for the flow reaches statistical steady state is plotted in Figure 9. The computed average value of C_d is 0.671, with an oscillation amplitude of 3.7×10^{-3}.

According to Figure 10, in additional to the Strouhal frequency, there is a second, though much smaller peak in the spectra at twice the Strouhal frequency. Johnson and Patel also reported this phenomenon.

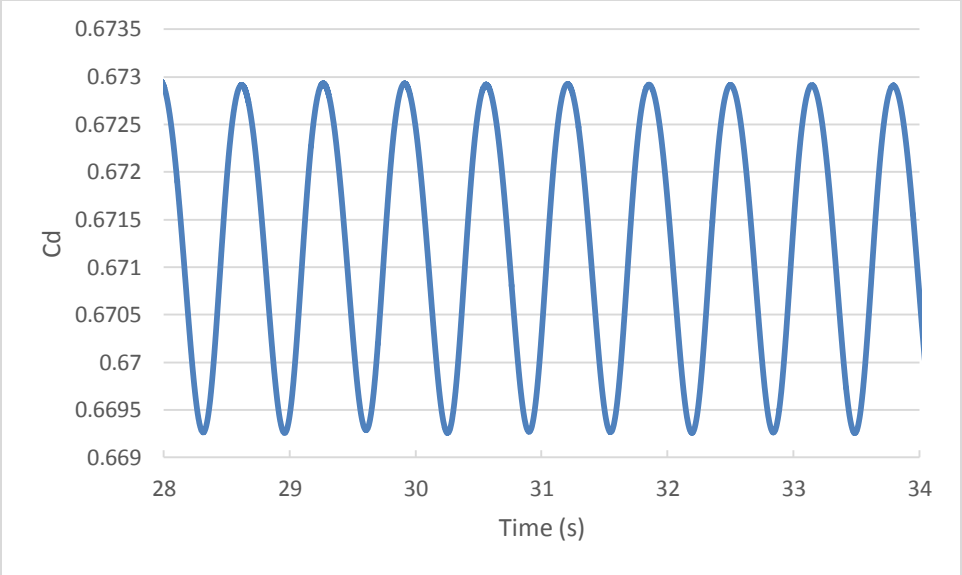

Figure 9. Time history of drag coefficient of Re = 300.

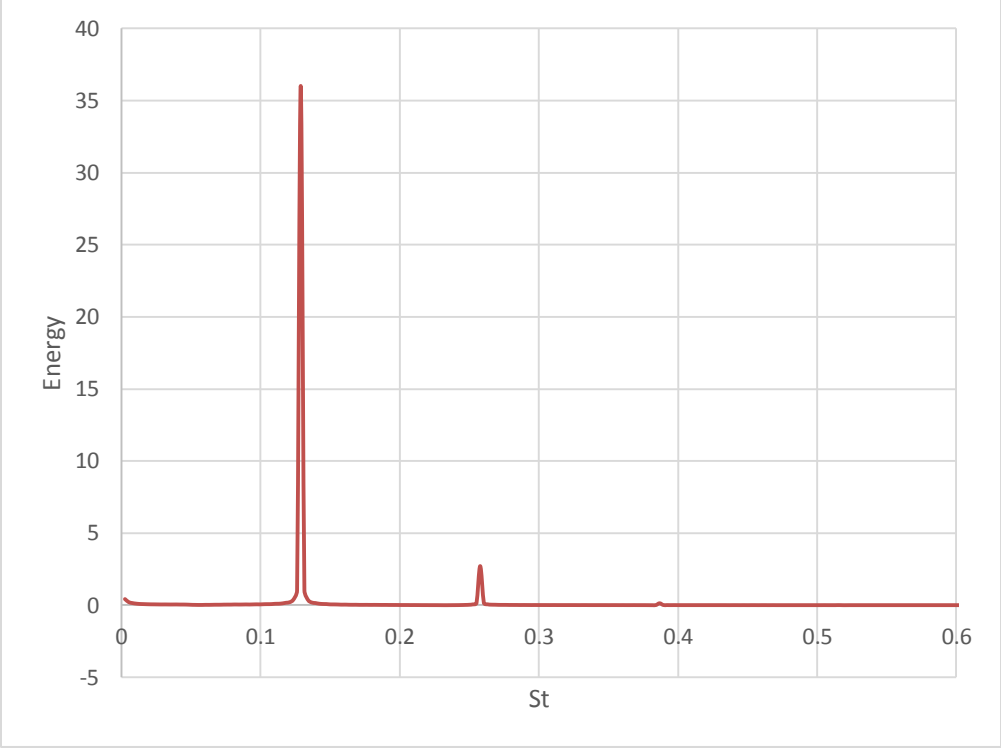

Figure 10. Power spectrum of drag coefficient of Re = 300.

3.1.4 Time averaged flow

Due to the planar symmetry in the vortex shedding process, the time-averaged flow at Re=300 is not axisymmetric. The streamwise velocity along the axis for the time-averaged flow is plotted in Figure 11. In the figure, x=0 is in the rear point of the sphere. For the average flow, the end of the recirculation region along the axis is at 1.3 diameters downstream from the rear point of the sphere.

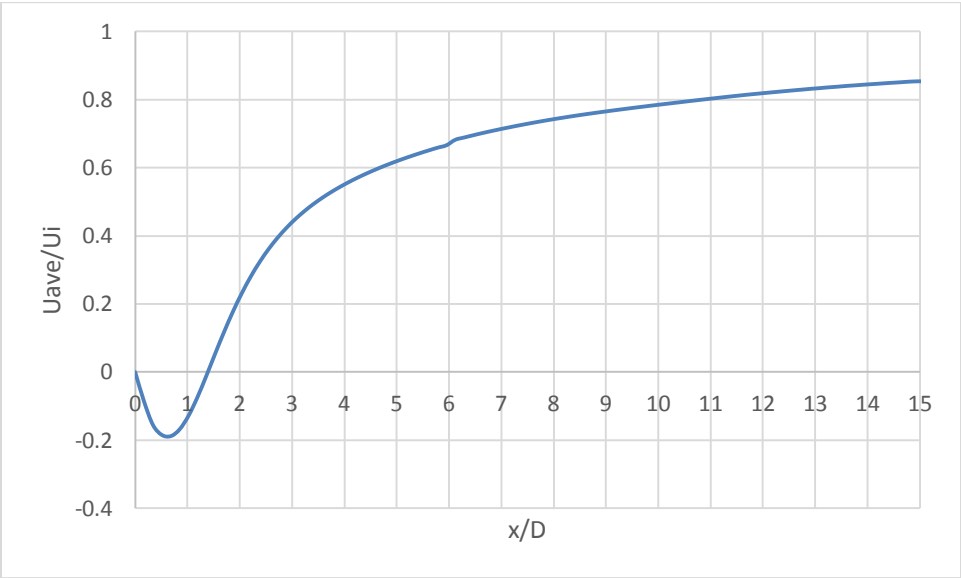

Figure 11. Average streamwise velocity along the axis of Re = 300.

3.1.5 Issues that influence the result

3.1.5.1 Blockage ratio

The blockage ratio is defined as the sphere's frontal area divided by the computational grid's frontal area. Smaller blockage ratio indicates less effects of boundary condition on the result.

According to my simulation, larger blockage ratio will make the drag coefficient C_d larger. In the above simulation, the blockage ratio is 0.18% and C_d =0.671. But C_d would be 0.698 if the blockage ratio increases to 3.14%, while mesh resolution and other parameters keep the same. This is in agreement with Jones and Clarke's analysis [12], who found Johnson and Patel [11] get C_d =0.656 with blockage ratio of 0.11%, while Tomboulides [32] get C_d =0.671 with blockage ratio of 1.23%.

3.1.5.2 Numerical scheme

The above simulation uses fourth order scheme is space and second order scheme in time. It provides a result of C_d =0.671 and St=0.129. It is better than the simulation using second order scheme in space and first order scheme in time with other parameters keeps the same, which gives C_d =0.687 and St=0.125.

3.1.5.3 Mesh density

For the flow past a sphere at Re=300, it is near the transition point from steady state to periodic state with vortex shedding. So the simulation result is sensitive to numerical issues. In my simulation, it is necessary to keep the mesh resolution large enough for appearance of periodic state. Otherwise, the final state will remain steady state even if it is unphysical.

Mesh density also has an effect on the value of drag coefficient. Lower density will make C_d decrease to some degree.

3.2 Numerical results at Reynolds number of 500

3.2.1 Flow pattern

A direct numerical simulation was performed at Re=500. At this Reynolds number, it is unnecessary to add random noise at the inlet. The flow becomes three-dimensional and results in vortex shedding by itself.

Isosurfaces of streamwise vorticity are plotted in Figure 12 to visualize the vortex structure. The red and blue colors correspond to positive and negative streamwise vorticity with the same magnitude.

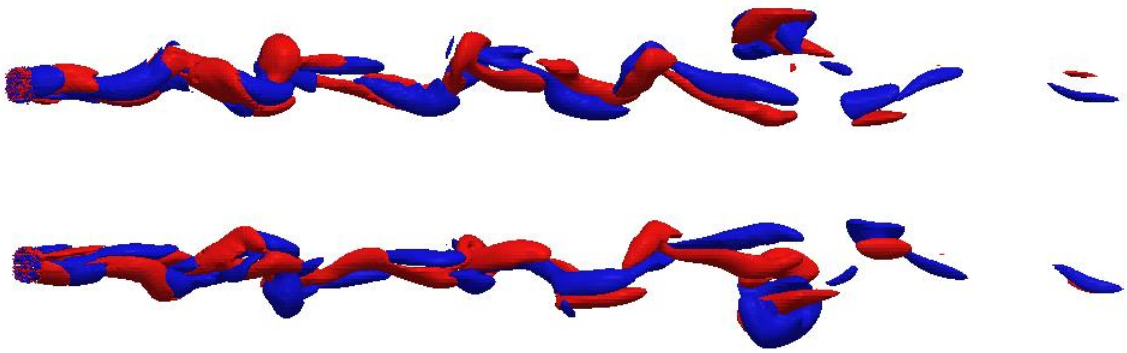

Figure 12. Isosurfaces of streamwise vorticity at one instant of time of Re = 500.

3.2.2 Drag coefficient and Strouhal number

The result of the drag coefficient for the flow reaches statistical steady state is plotted in Figure 13. The computed average value of C_d is 0.559, with an oscillation about 0.03.

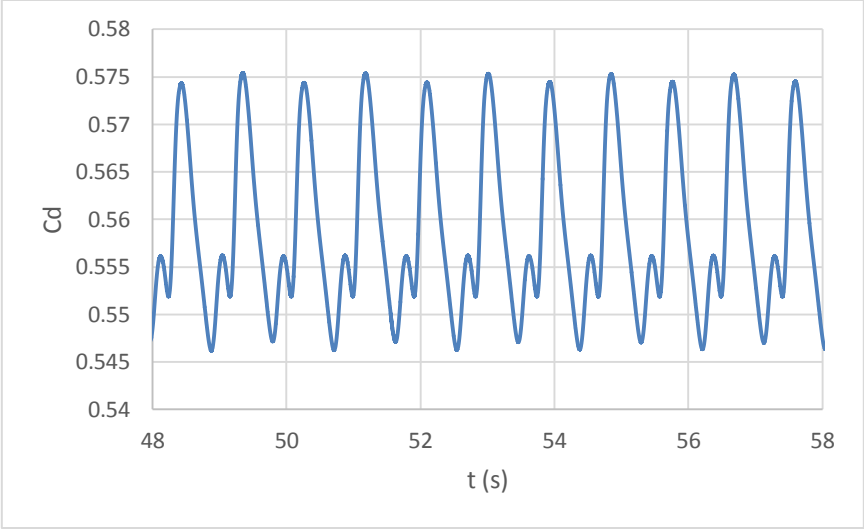

Figure 13. Time history of C_d at Re = 500.

Figure 14(a) shows the velocity component in x direction at the location of 2 diameters downstream the sphere in the axis. There are four peaks in the frequency domain in Figure 14(b). The two main peaks are at the Strouhal number of 0.054 and 0.163.

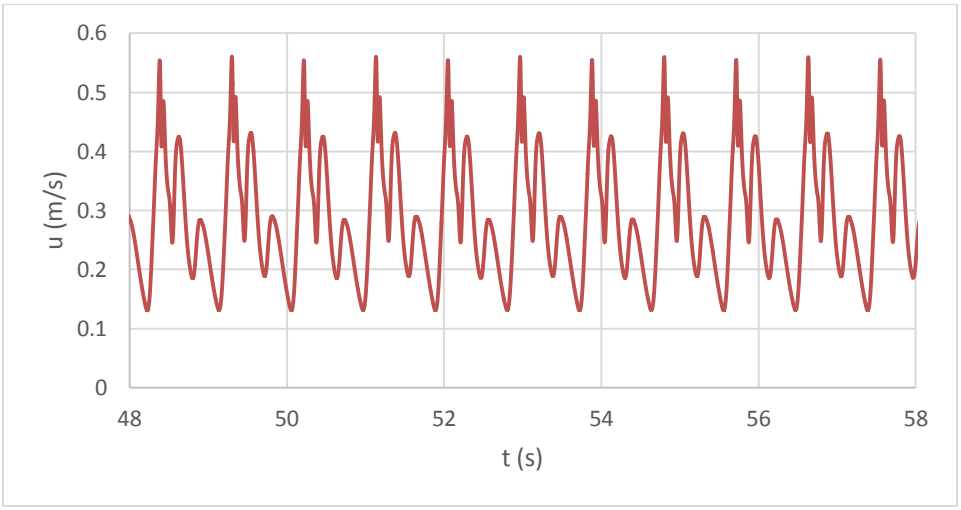

(a)

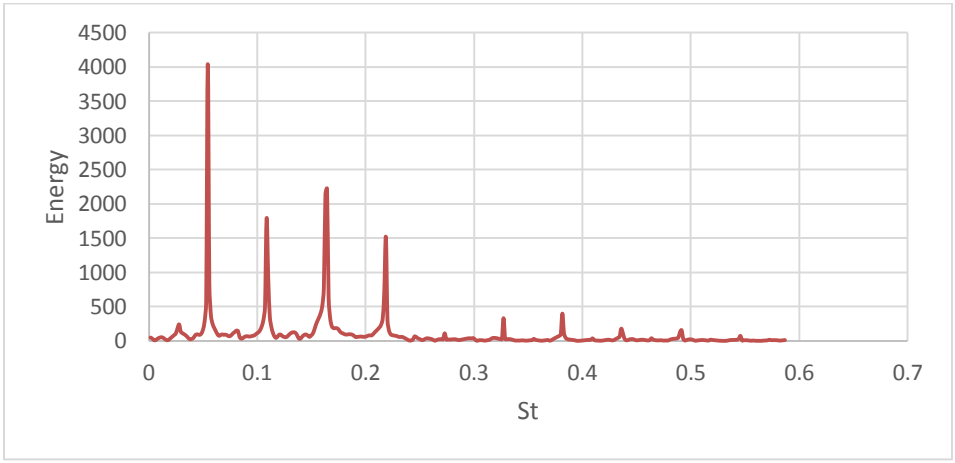

(b)

Figure 14. (a) Time history of streamwise velocity and (b) its power spectrum at the point of 2D downstream the sphere in the central axis

3.2.3 Visualization of vortex ring

At Re=500, vortex loops are shed from the sphere with different orientations. And these vortex loops reorganized into vortex rings in the downstream region of the wake. This phenomenon is reported by the experiment of Margavey and Bishop [15].

To visualize the vortex rings, the isosurface of the magnitude of vorticity is plotted in Figure 14 when flow is statistically steady. It is evident that the vortex rings are formed in the downstream region. To confirm this, in Figure 16 the vector v1 is plotted for the vortex ring in the right side of Figure 15, while v1 is the velocity vector v subtracted by 95% of the inlet flow velocity. The velocity vectors v1 wrap around the ring, which verifies the existence of vortex rings.

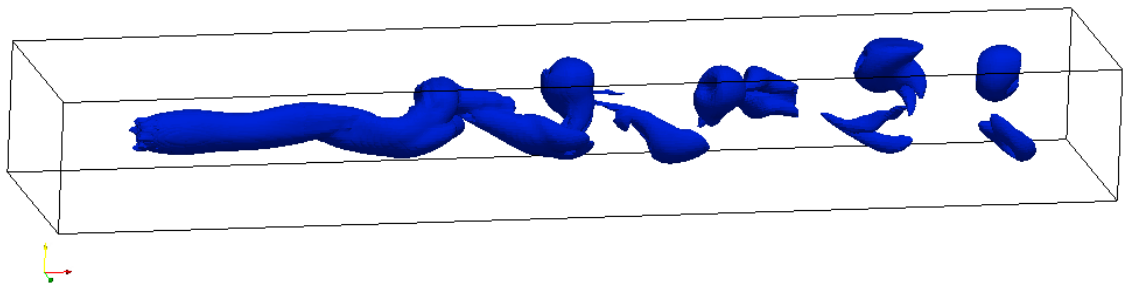

Figure 15. Isosurface of vorticity magnitude of Re = 500.

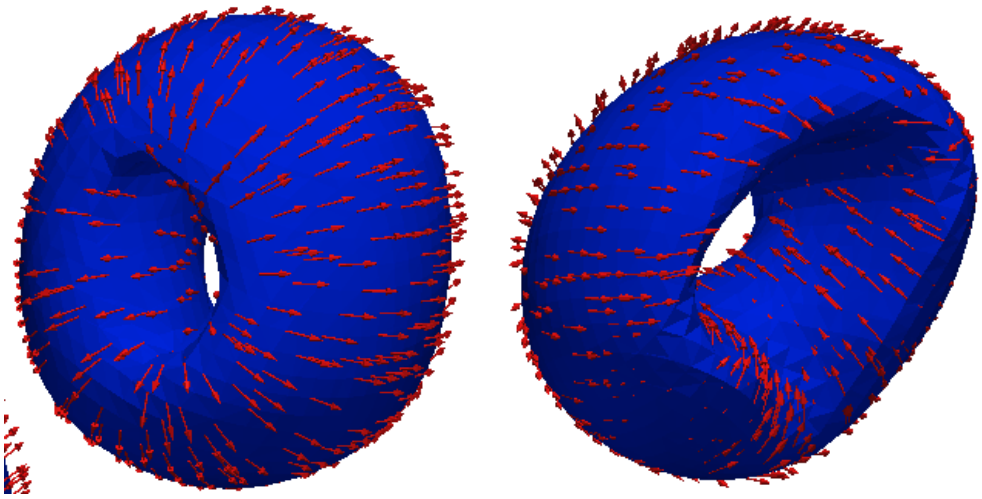

Figure 16. Different views of vortex rings

3.3 The surface signature at Reynolds number of 500

3.3.1 Surface signature

The wake will attach the surface in a shorter distance if the sphere is closer to the surface. In this case, the sphere is moved to the location that the top of the sphere is 1 diameter to the surface. The computational domain is shown in Figure 17.

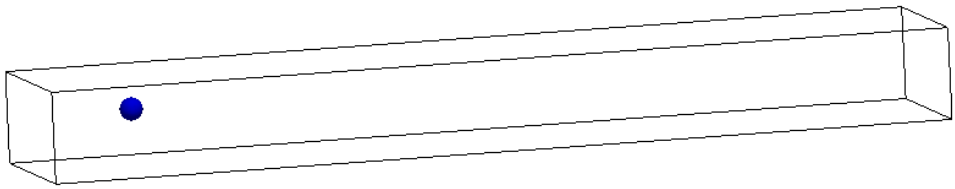

Figure 17. Numerical domain for the simulation of surface signature of Re = 500.

On the surface, periodic regions appear on the surface of the flow for the velocity magnitude field in Figure 18. The velocity in these regions is lower than the surroundings.

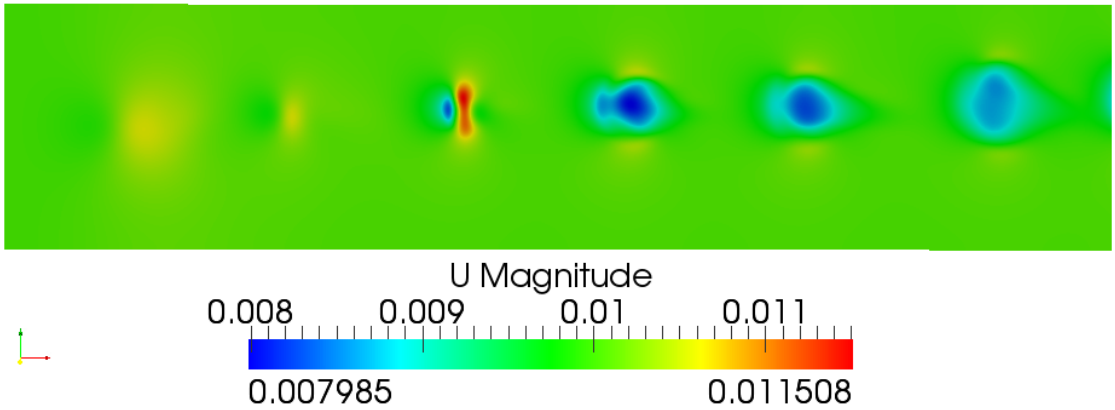

Figure 18. Velocity magnitude on the surface of Re = 500.

Constant heat flux is performed towards the top surface. According to Figure 19, the temperature of flow surface gradually increases from the inlet due to the heat flux. Those periodic regions appear again on the surface with lower temperature, which indicates that the cold flow is from the wake below the surface. Those are the thermal surface signatures.

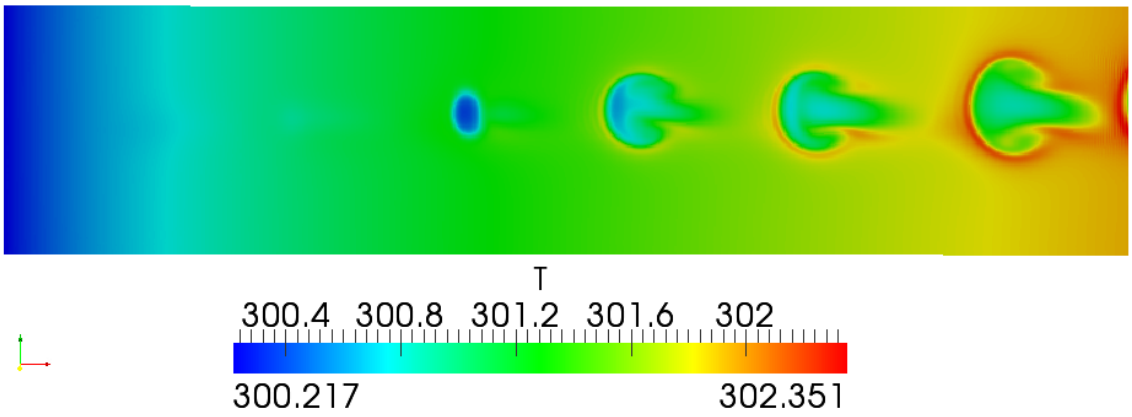

Figure 19. Temperature on the surface with constant heat flux of Re = 500.

3.3.2 Pattern of the signature

In the cold regions, there is a pair of vortices with opposite directions of rotation. It can be visualized by plotting vector $\boldsymbol{v_1} = \boldsymbol{v} - 0.95\boldsymbol{v_{inlet}}$ in Figure 20, where $\boldsymbol{v}$ is the velocity vector and $\boldsymbol{v_{inlet}}$ is the inlet velocity vector.

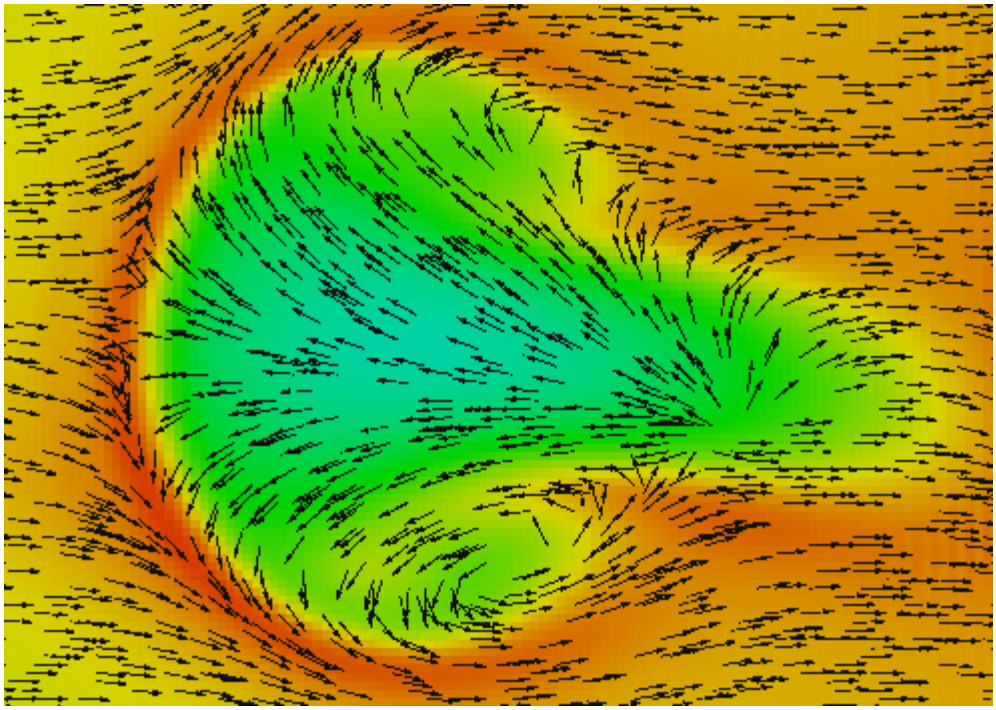

Figure 20. Velocity vector $\boldsymbol{v_1}$ in the surface signature.

This phenomenon can also be visualized by putting passive particles on the surface in Figure 21. There are only a few particles remaining in the cold regions. Their moving trajectory shows the rotation of the two vortices.

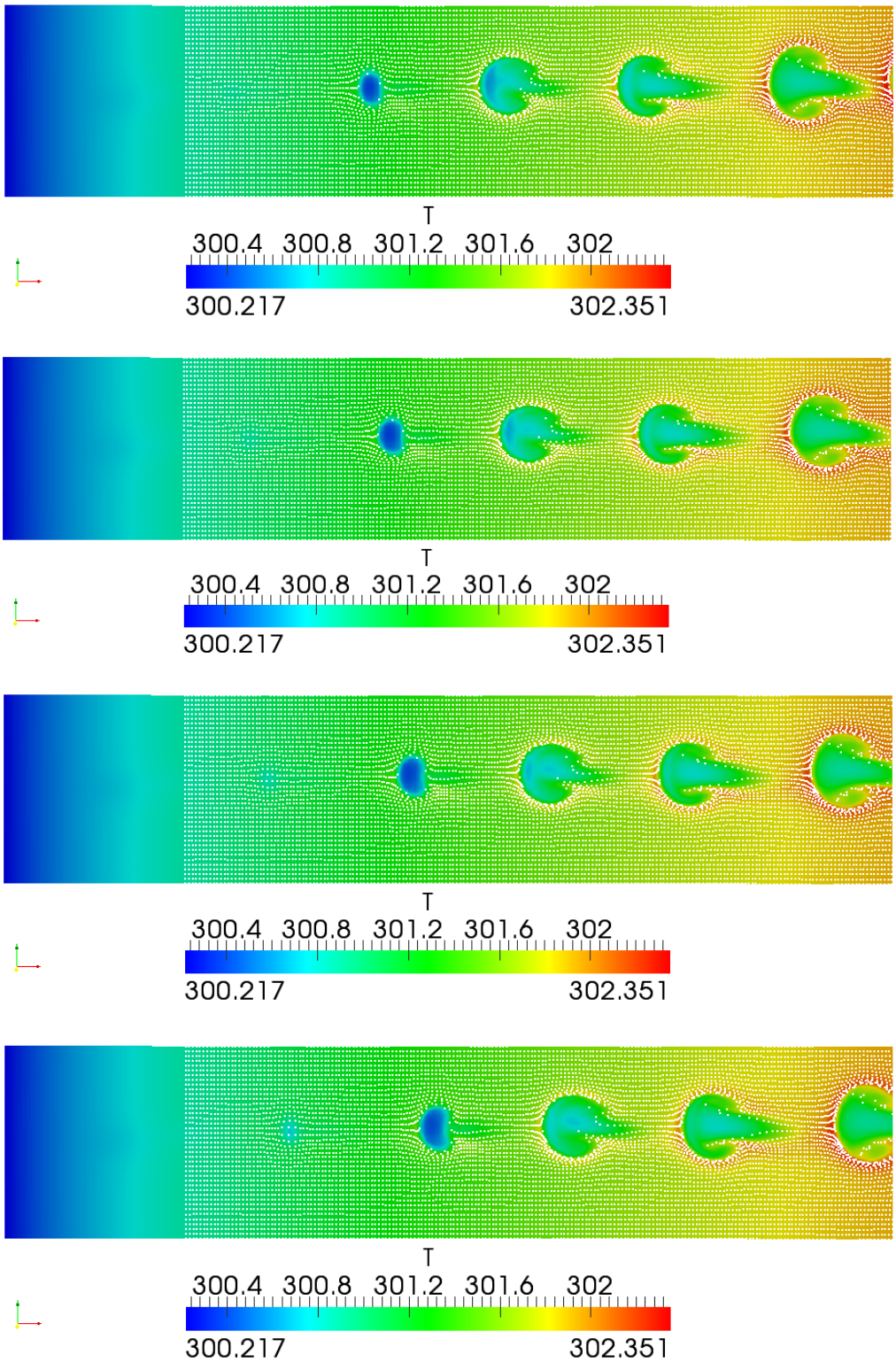

Figure 21. Passive particles on the surface at different instants of time of Re = 500.

4. ANALYSIS AND DISCUSSION

4.1 Flow at Reynolds number of 300

4.1.1 Flow pattern

The transition from steady to unsteady flow happens between Re=270 and Re=290 for flow past a sphere, according to almost all the numerical and experimental results. So for Re=300, the flow should be periodic with vortex shedding.

Tomboulides and Orszag [31] report that the flow at Re=300 maintains planar symmetry around the plane on which the vortex shedding happens, while the axial symmetry is already lost. To prove this, isosurfaces of streamwise vorticity are plotted in Figure 22, which show that the vortex loops are always shed from the sphere with the same orientation. It is in agreement with the result of Tomboulides and Orszag [31] in Figure 23. Similar pattern was also described by Achenbach [1].

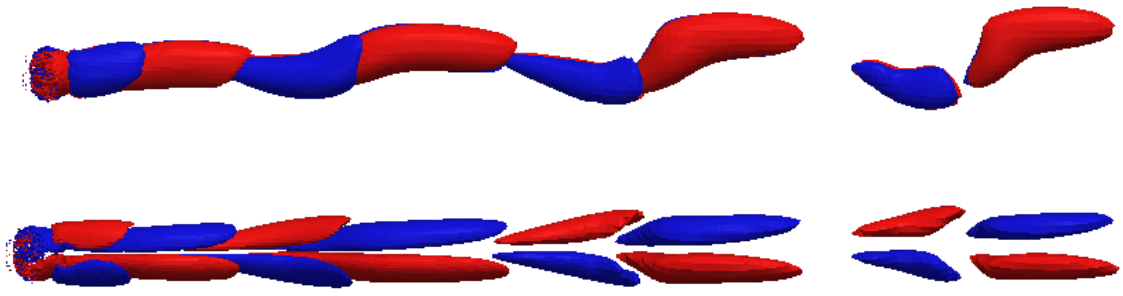

Figure 22. OpenFOAM: isosurfaces of streamwise vorticity at Re = 300.

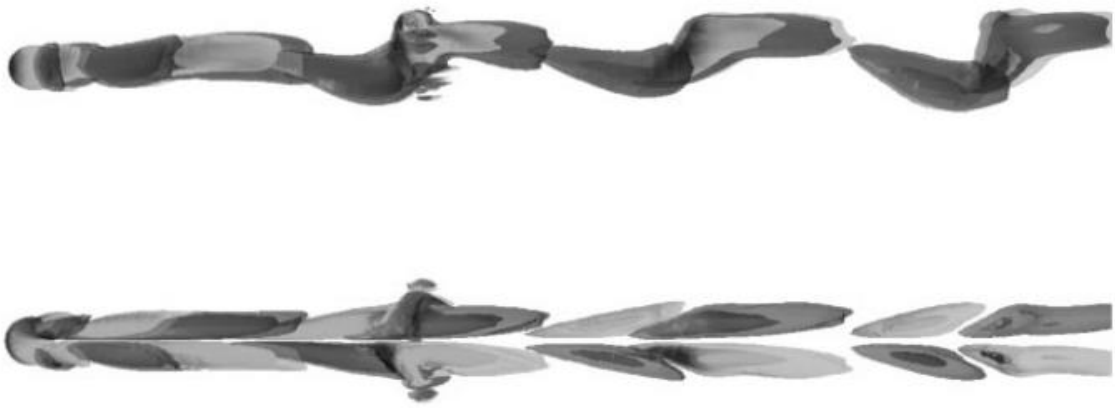

Figure 23. Tomboulides and Orszag: isosurfaces of streamwise vorticity at Re = 300.

4.1.2 Comparison of drag coefficient and Strouhal number

For flow past a sphere at Re = 300, the result of the drag coefficient and its power spectrum is plotted in Figure 24. The computed average value of C_d is 0.671, with an oscillation amplitude of 3.7×10^{-3}.

The experimental data of Roos & Willmarth [27] gave an interpolated value for C_d at Re=300 of 0.629. Johnson and Patel provided C_d =0.656 with an oscillation amplitude of about 6.7×10^{-3} in their numerical simulation. Tomboulides [32] found C_d =0.671 with an oscillation amplitude of about 2.8×10^{-3} using direct numerical simulation with a mixed spectral element/Fourier spectral method. Ploumhans [25] used three-dimensional vortex methods to simulate the flow past a sphere at Reynolds numbers of 300, 500 and 1000. At Re = 300 they found that the flow attained a time periodic regime with a mean value for C_d of 0.683 with an oscillation of 2.5×10^{-3}. Jones and Clarke [12] found C_d = 0.668 using Fluent.

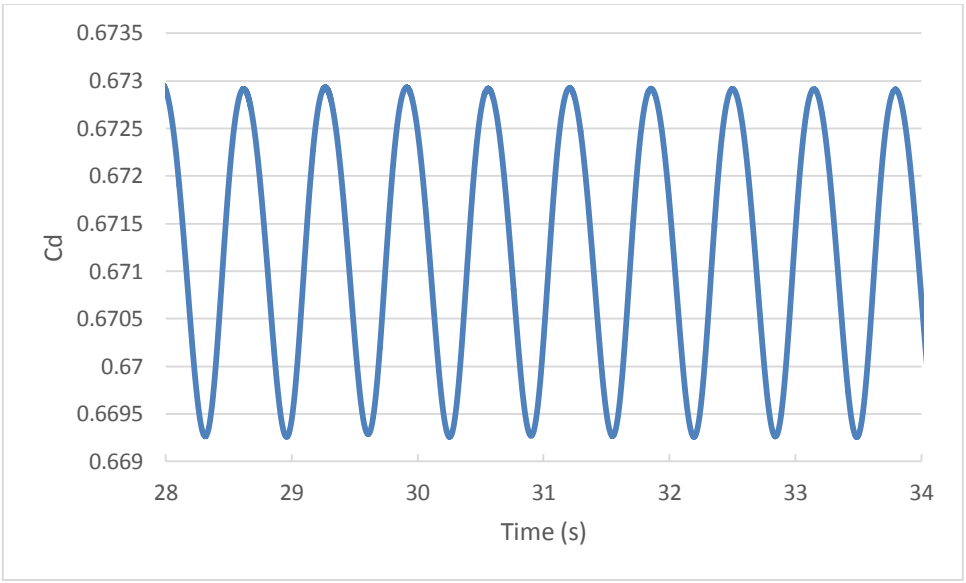

(a)

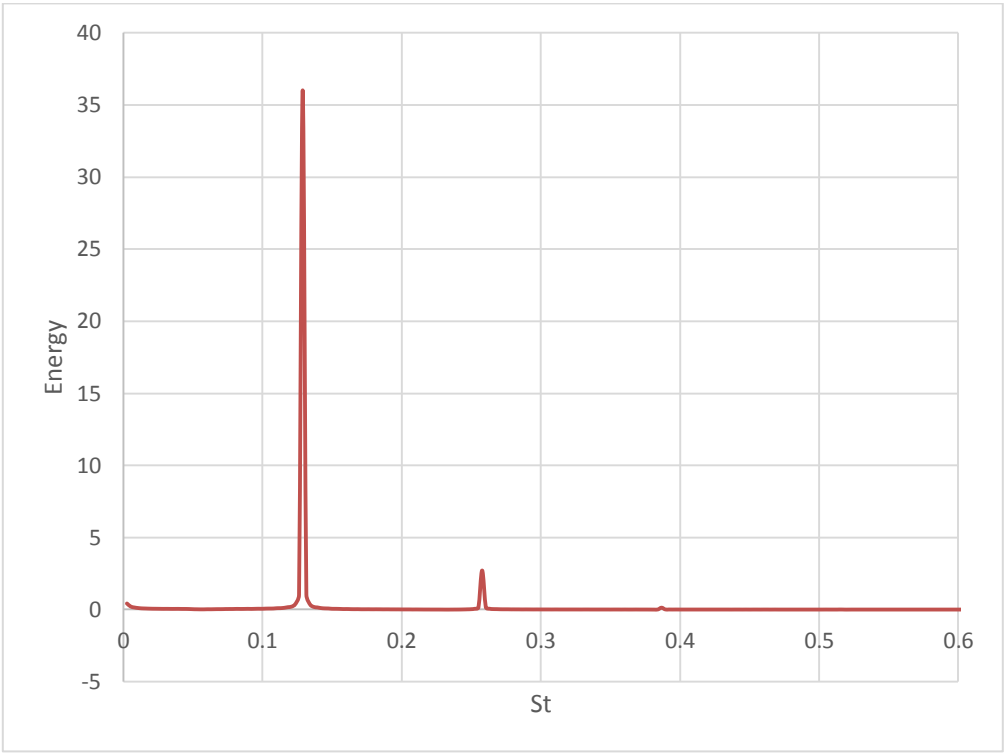

(b)

Figure 24. (a) Time history of drag coefficient and (b) its power spectrum of Re = 300.

For the Strouhal number, there is a dominant peak indicating at 0.129. Johnson and Patel [11] reported the Strouhal number to be 0.137. Tomboulides [32] gave a number of 0.136. Ploumhans [25] found the Strouhal number to be 0.135. Jones and Clarke [12] provided a number of 0.133 using Fluent. The simulation results of present work are compared with those previous results in Table 3.

Table 3. Comparison of results of present work with other results at Re = 300

	C_d	Oscillation of C_d	St
OpenFOAM	0.671	1.9×10^{-3}	0.129
others	0.629 [10] 0.656 [4] 0.671 [14] 0.683 [9] 0.668 [29]	3.5×10^{-3} [4] 2.8×10^{-3} [14] 2.5×10^{-3} [9]	0.137 [4] 0.136 [14] 0.135 [9] 0.133 [29]

4.1.3 Convergence study

The mesh density can influence the result according to the discussion in 3.1.5. To prove the convergence of the above results, cases with different mesh resolution are calculated while other parameters are kept the same.

The averaged drag coefficient C_d is plotted for the cases with different mesh resolutions in Figure 25.

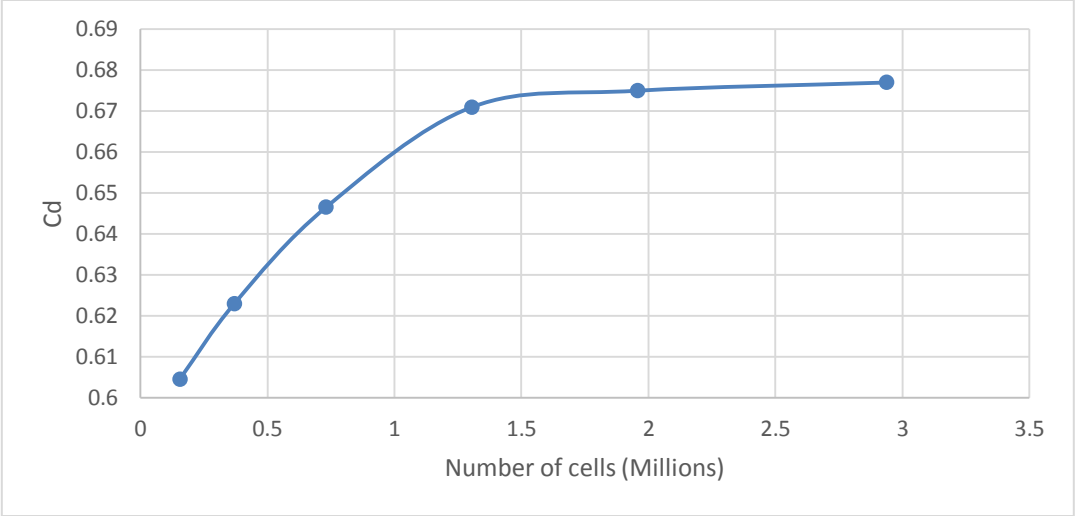

Figure 25. The averaged drag coefficient at different mesh resolution

According to Figure 24, the averaged C_d increases as mesh density increases. But the averaged C_d barely changed when the number of cells exceeds 1.3 million. So we can consider the solution to be independent of mesh at cell level of 1.3 million. High mesh resolution means much longer time of computation. Hence the mesh with about 1.3 million cells is used.

4.2 Flow at Reynolds number of 500

4.2.1 Flow pattern

The wake structure at Re = 500 is similar with the one at Re=300. But vortex loops are shed from the sphere with different orientations at Re=500, instead of shed from the same orientation at Re=300. The planar symmetry at Re=300 is no longer preserved at Re=500. To prove this, the isosurface of streamwise vorticity is plotted in

Figure 26, where red and blue colors correspond to positive and negative value with the same magnitude. And the figure is compared with the results of Tomboulides and Orszag [31] in Figure 27.

The transition from a one-frequency flow to an almost chaotic system occurs at around Re=420 (Sakamoto and Haniu [28]). Tomboulides and Orszag [31] reported that there was a lower incommensurate frequency of around 0.045 associated with the loss of planar symmetry. It is related with the irregular rotation of the separation point azimuthally around the rear part of the sphere, which results in a more complicated wake structure in Figure 26.

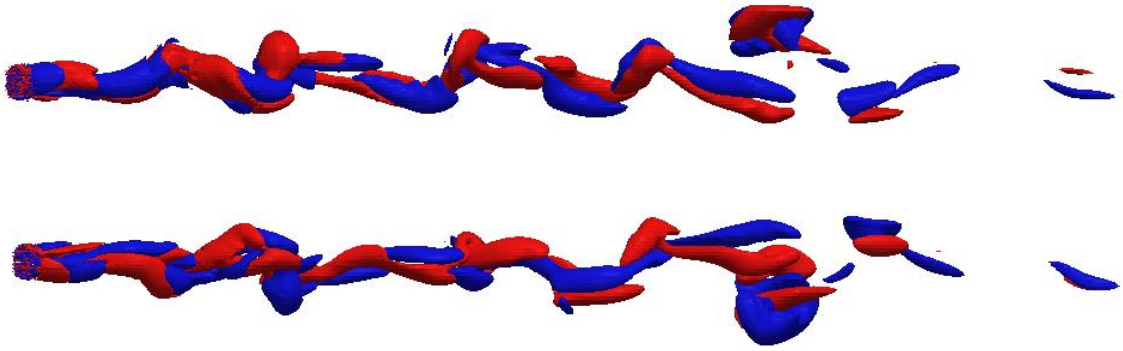

Figure 26. OpenFOAM: isosurfaces of streamwise vorticity at Re = 300.

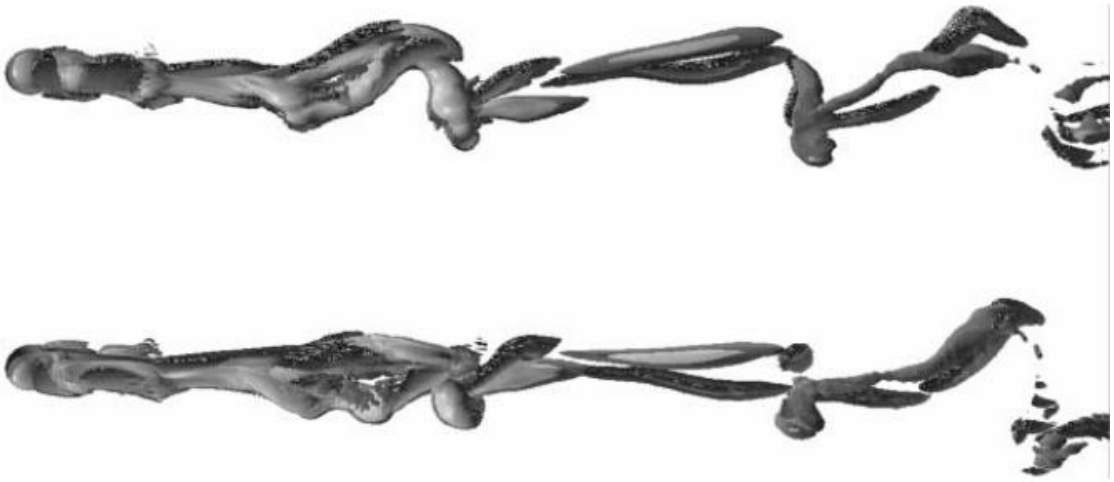

Figure 27. Tomboulides and Orszag: isosurfaces of streamwise vorticity at Re = 300.

4.2.2 Comparison of drag coefficient and Strouhal number

For flow past a sphere at Re = 300, the result of the drag coefficient is plotted in Figure 28. The computed average value of C_d is 0.559, with an oscillation amplitude of 0.03. The experimental data of Roos & Willmarth [27] gave a value for C_d at Re=500 of 0.547. Ploumhans [25] got the average value of C_d at about 0.58.

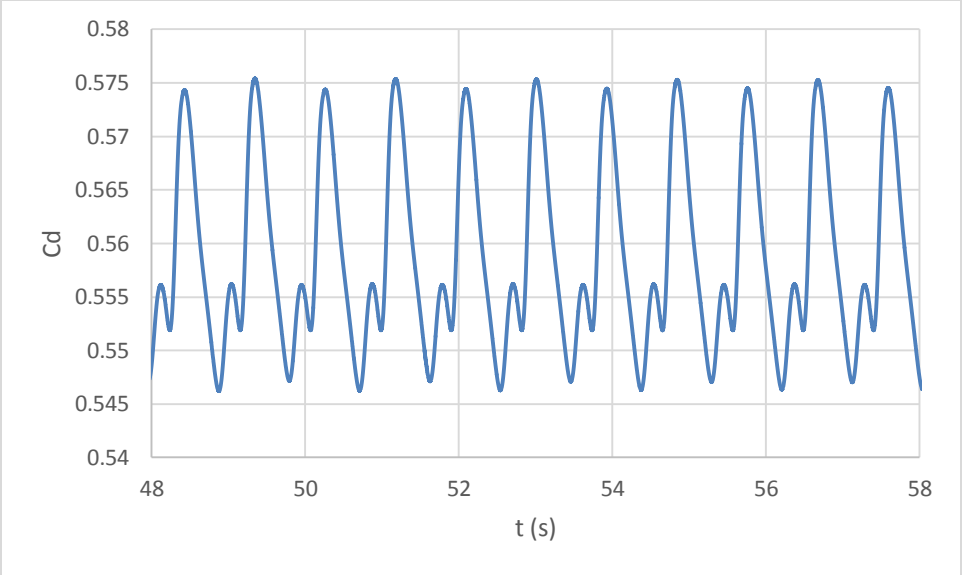

Figure 28. Time history of drag coefficient of Re = 500.

Figure 29 shows the velocity component in x direction at the location of 2 diameters downstream the sphere in the center line. The result of Strouhal number is in Figure with two main peaks at 0.054 and 0.163. Figure 30 shows the results of Tomboulides and Orszag [31] at the same location. Their velocity is more chaotic than the velocity in the present work in Figure 29, which result in the lower energy for the lower frequency of St = 0.045. A possible reason of this difference is that Tomboulides and Orszag [31] used mixed spectral element/Fourier spectral method, which is a very high order numerical method with nearly no numerical dissipation.

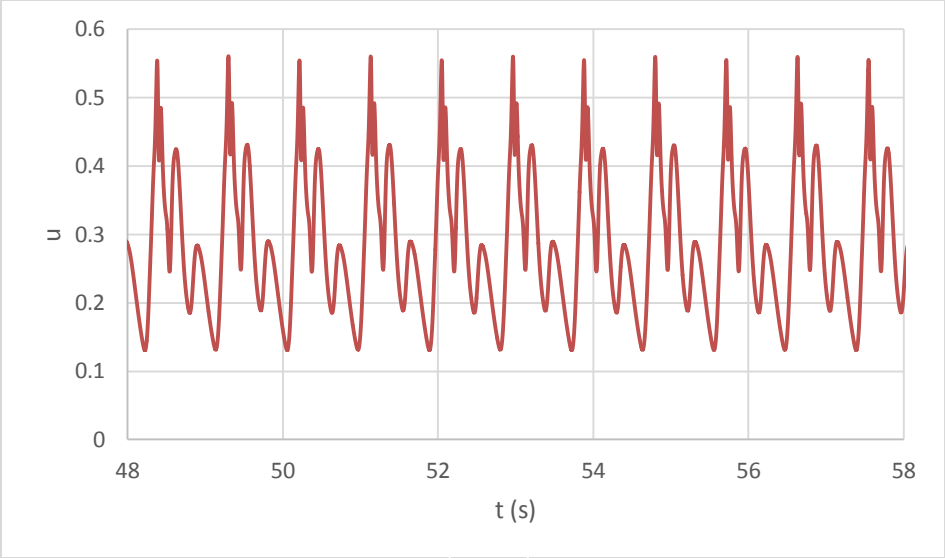

(a)

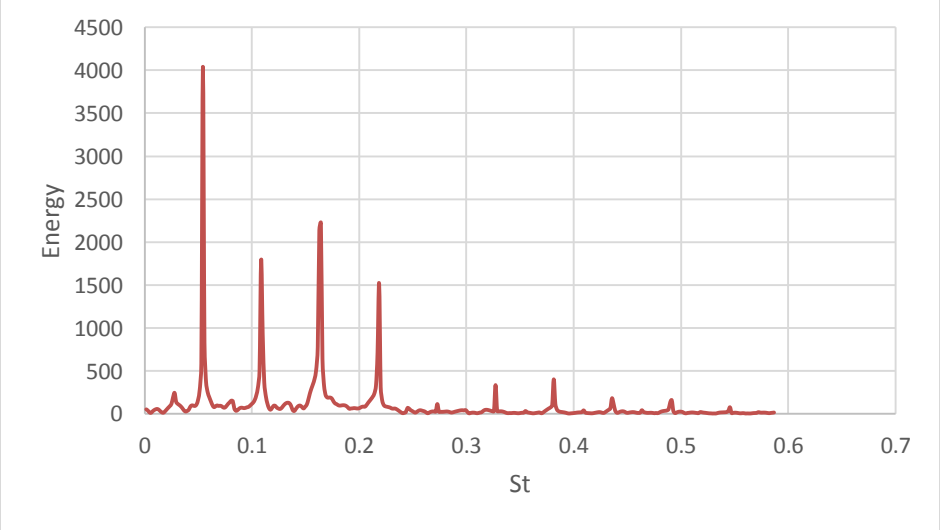

(b)

Figure 29. OpenFOAM: (a) Time history of streamwise velocity and (b) it power spectrum at 2D downstream the sphere in the axis of Re = 500.

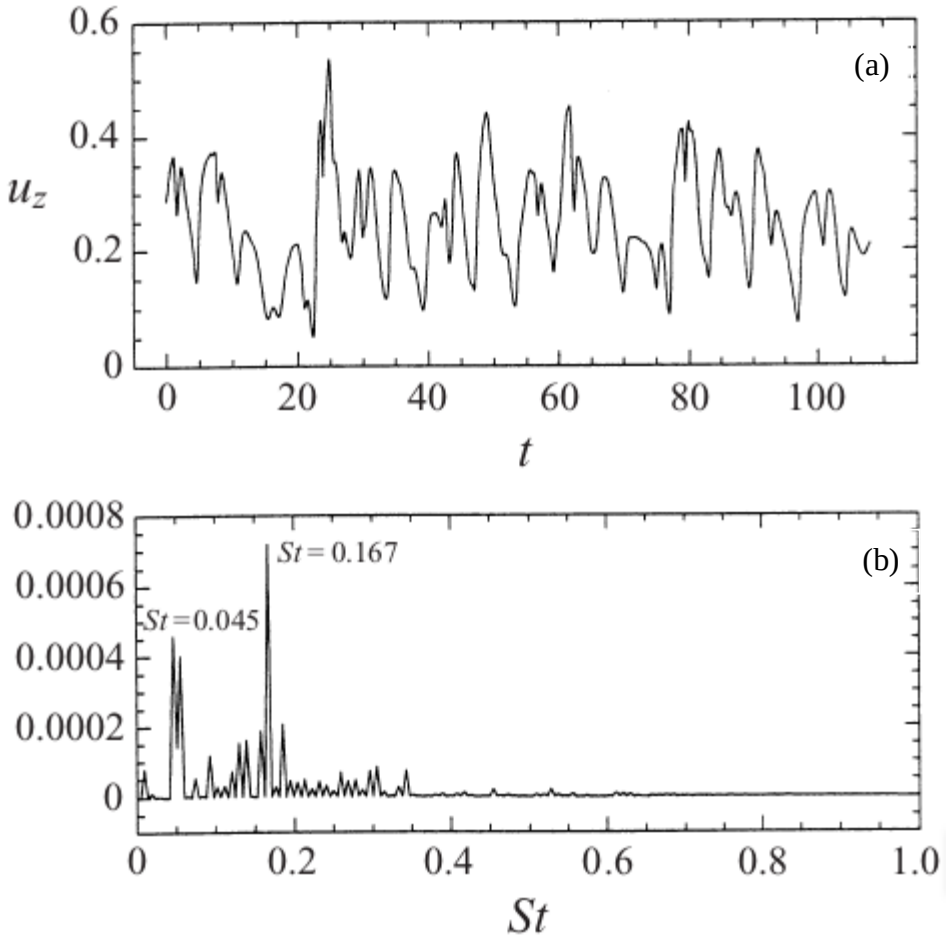

Figure 30. Tomboulides and Orszag: (a) Time history of streamwise velocity and (b) it power spectrum at 2D downstream the sphere in the axis of Re = 500.

4.3 Surface signature at Reynolds number of 500

4.3.1 Formation of vortex rings

Figure 31 shows the time-averaged velocity field in x direction at Re = 500. It is evident that the velocity in x direction u of the wake region is lower than the average velocity. The distribution of u of the wake region is given in Figure 32(a). Then the z component of vorticity distribution of the wake region is plotted in Figure 32(b).

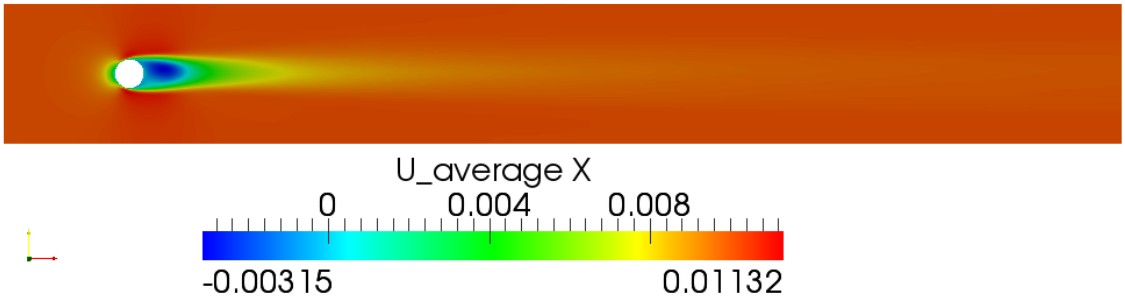

Figure 31. Side view of time-averaged streamwise velocity at Re = 500.

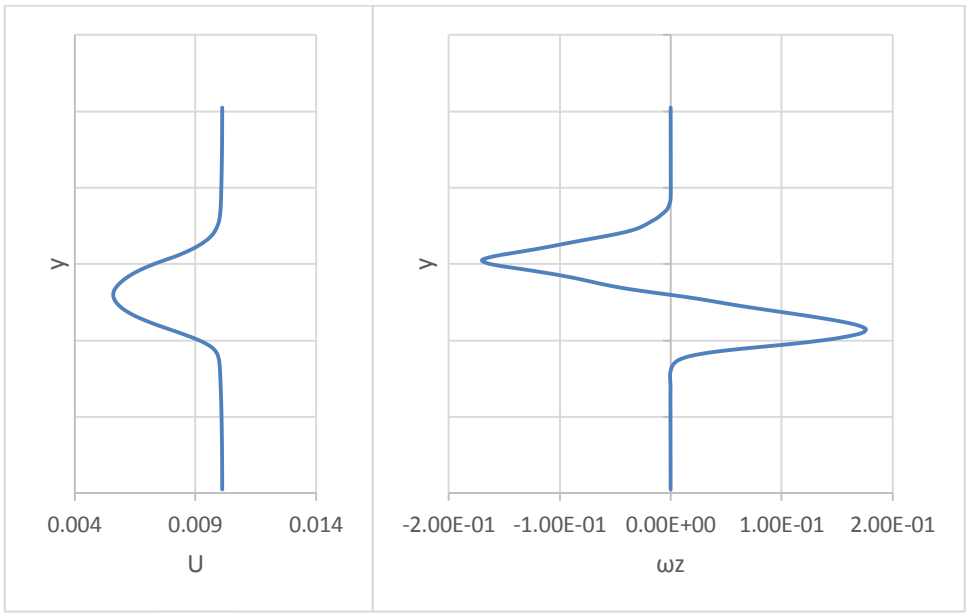

(a) (b)

Figure 32. (a) Streamwise velocity and (b) vorticity in z direction distribution in the wake region along y axis.

A cylindrical vortex sheet forms according to the vorticity distribution. Due to the instability effect, the cylindrical vortex sheet is reorganized into vortex rings as can be observed from Figure 33.

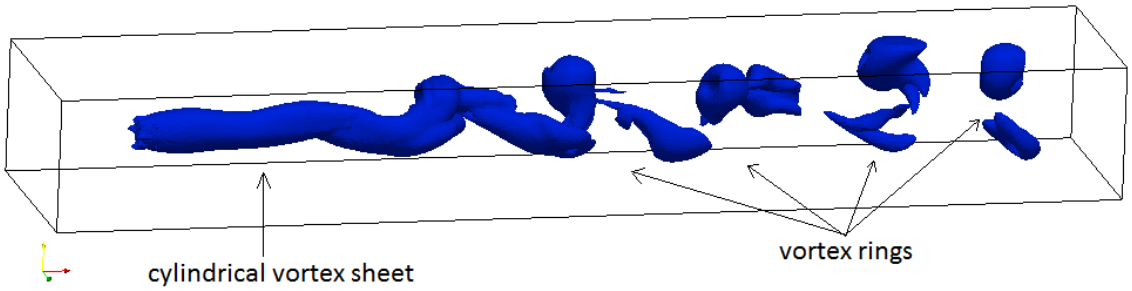

Figure 33. Isosurface of vorticity magnitude of Re = 500.

4.3.2 Vortex rings to the surface

The vortex rings are formed in the downstream region of the wake at Re = 500. When the sphere is relatively close to the surface, those vortex rings will attach the surface in Figure 34. Then they are deformed and become incomplete rings in Figure 33. The attachment between the vortex rings and the surface results in the two vortices in the surface signature according to Figure 35.

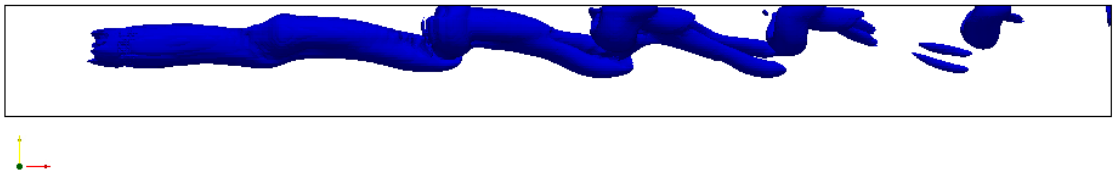

Figure 34. Isosurface of vorticity magnitude of Re = 500 when the sphere is 1D under the surface.

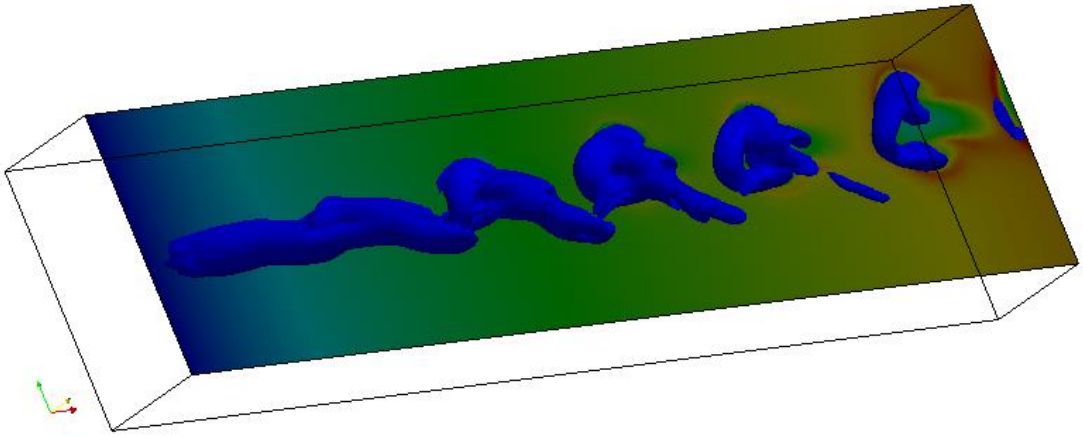

Figure 35. Vortex rings attaching the surface.

4.3.3 Particle visualization

It is interesting that many particles accumulate on the edge of cold regions, only a few can enter. This can be explained. Sitting on the edge of a cold region, the flow on the left side has large velocity than the flow on the right side, according to Figure 34. So if the edge is regarded as the reference frame, the flow on either side will move towards it and sink, see Figure 37. On the surface, the velocity will gradually decrease to zero on either side. Particles on the surface can only remain on the surface. So they will remain

on the edge when they come from other locations since their velocity already become zero.

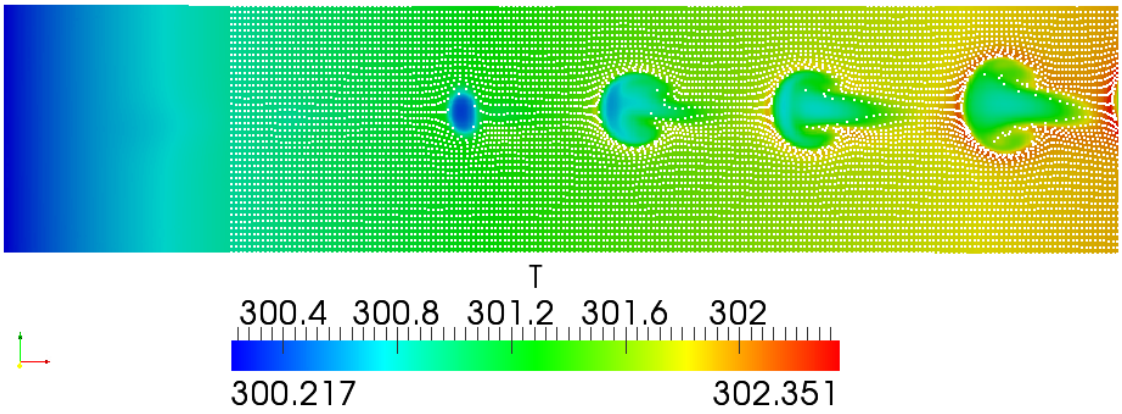

Figure 36. Temperature field with particles on the surface of Re = 500.

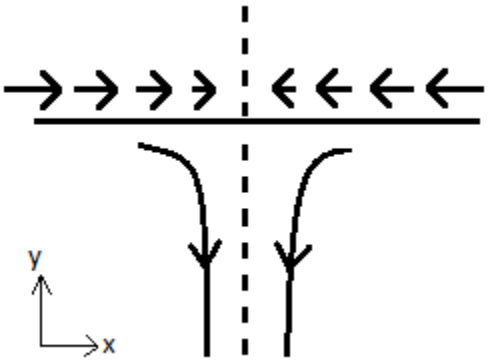

Figure 37. Velocity in the leading edge of signature.

This phenomenon can also be explained by the convergence and divergence theory. When surface divergence happens, the flow moves upward to the surface and

diverges, see Figure 36. When surface convergence happens, the flow converges from all the directions on one point and then goes down, see Figure 37.

In this case, the surface divergence happens in the center of the cold regions, where cold flow moves up towards the surface as shown in Figure 38. And surface convergence happens on the edge of the cold regions, where flow from either side moves toward the edge and goes down as shown in Figure 39.

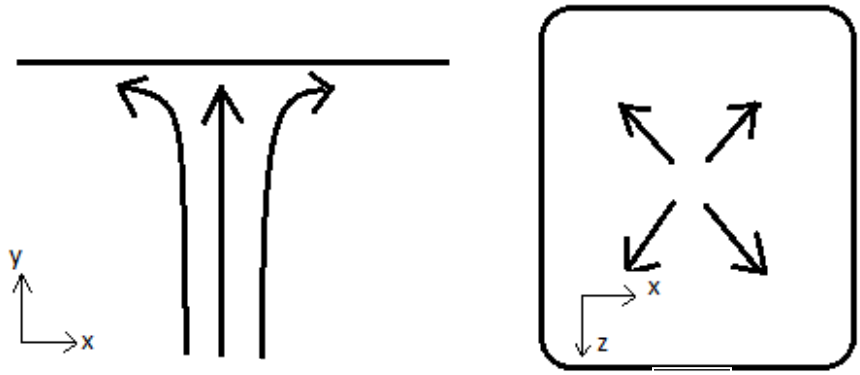

(a) (b)

Figure 38. Velocity in divergent region (a) side view (b) top view.

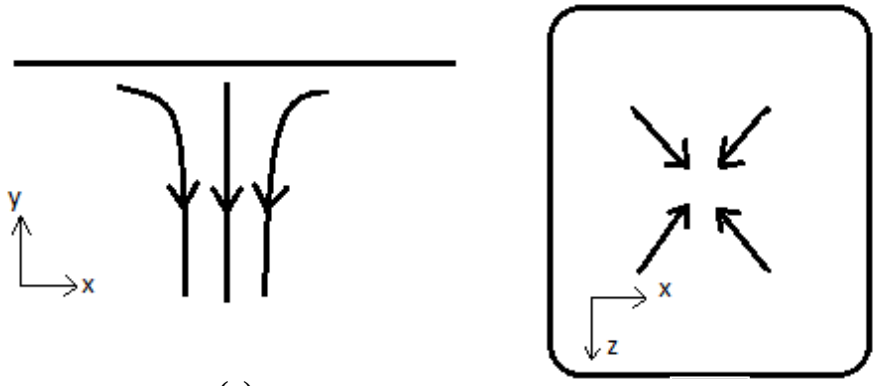

(a) (b)

Figure 39. Velocity in convergent region (a) side view (b) top view.

Consider the mass conservation equation,

$$\frac{\partial u}{\partial x}+\frac{\partial v}{\partial y}+\frac{\partial w}{\partial z}=0 \tag{4.1}$$

On the surface,

$$\frac{\partial u_s}{\partial x}+\left(\frac{\partial v}{\partial y}\right)_s+\frac{\partial w_s}{\partial z}=0 \tag{4.2}$$

$$\left(\frac{\partial \mathrm{v}}{\partial \mathrm{y}}\right)_s=-(\frac{\partial \mathrm{u_s}}{\partial \mathrm{x}}+\frac{\partial \mathrm{w_s}}{\partial \mathrm{z}}) \tag{4.3}$$

$$(\nabla\cdot\boldsymbol{v})_s=-\left(\frac{\partial v}{\partial y}\right)_s \tag{4.4}$$

On divergent point, flow going up and the velocity decreases to zero on the surface.

$\left(\frac{\partial v}{\partial y}\right)_s < 0$, $(\nabla \cdot \boldsymbol{v})_s > 0$

On convergent point, flow going down and the velocity decreases from zero on the surface.

$\left(\frac{\partial v}{\partial y}\right)_s > 0$, $(\nabla \cdot \boldsymbol{v})_s < 0$

The flow is incompressible. But for flow on the surface, $(\nabla \cdot \boldsymbol{v})_s \neq 0$, which makes it act like compressible flow. On divergent point, there seems to be a source of mass. On convergent point, there seems to be a sink of mass. This can explain why the particles accumulate on the edge, while nearly no particle is in the center of the cold region.

4.3.4 The hot edge of surface signature

It is also evident that the temperature of the edge is higher than the surroundings, according to Figure 40. It is an easy way to explain it using convergence theory. The surface convergence happens on the edge. There is a constant heat flux $\mathrm{Q} = -\mathrm{k}\frac{\partial \mathrm{T}}{\partial \mathrm{y}}$ towards the surface. So the slope $\frac{\partial \mathrm{T}}{\partial \mathrm{y}}$ remains constant. When surface convergence happens, the flow goes down. So the fluid particle in figure goes down. For a small amount of time, the temperature of the fluid particle can be considered constant. In order to remain the temperature gradient in y direction $\frac{\partial \mathrm{T}}{\partial \mathrm{y}}$ constant, the temperature on the surface will be higher as shown in Figure 41.

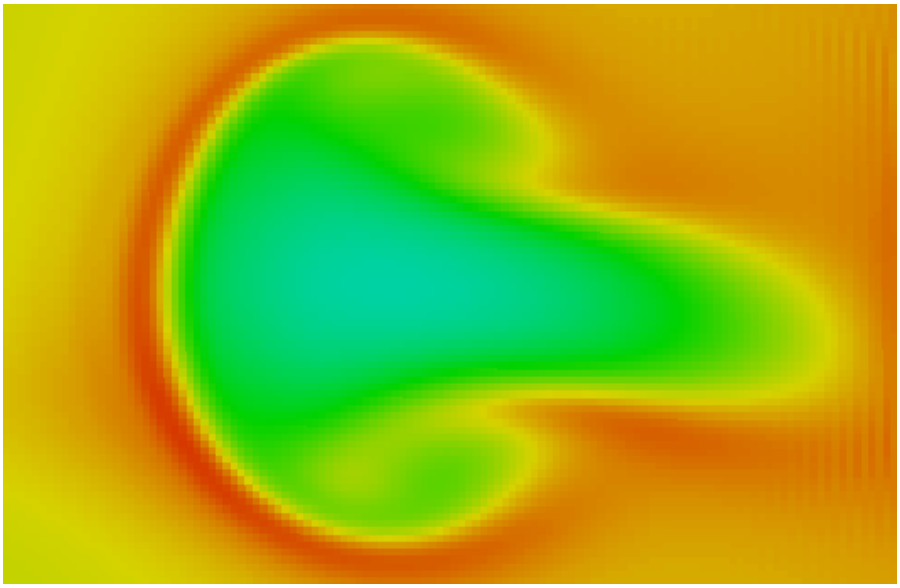

Figure 40. Temperature field of surface signature.

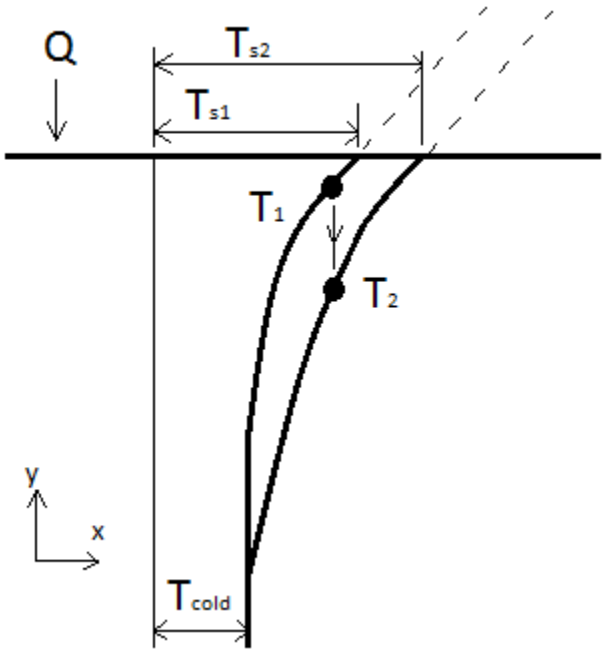

Figure 41. Side view of temperature distribution in convergent region.

4.3.5 The influence of physical and numerical parameters

4.3.5.1 Prandtl number

The Prandtl number Pr is a dimensionless number. It is the ratio of momentum diffusivity (kinematic viscosity) to thermal diffusivity.

It is defined as: $\Pr = \frac{\nu}{\alpha} = \frac{viscous\ diffsion\ rate}{thermal\ diffsion\ rate} = \frac{c_p \mu}{k}$, where α is the thermal diffusivity $\alpha = k/(\rho c_p)$.

When *Pr* is small, the heat diffuses more quickly compared to the velocity (momentum). In this case, the temperature field will look blurry.

Figure 42 shows the temperature field of the surface for flow past a flow with different Prandtl numbers. In these cases, the thermal conductivity is different, while other parameters keep the same, like kinematic viscosity, Reynolds number, heat flux and mesh density.

The thermal surface signature for Pr = 0.2 is the most blurry, while the one of Pr = 7 is the sharpest. But in the case of Pr =7, there is some numerical induced oscillations around the hot edge in Figure 43, where has the highest gradient of temperature. It is believed that the phenomenon is due to the Gibbs oscillation. For the cases with lower Prandtl numbers, there is no such oscillation because of the higher diffusivity.

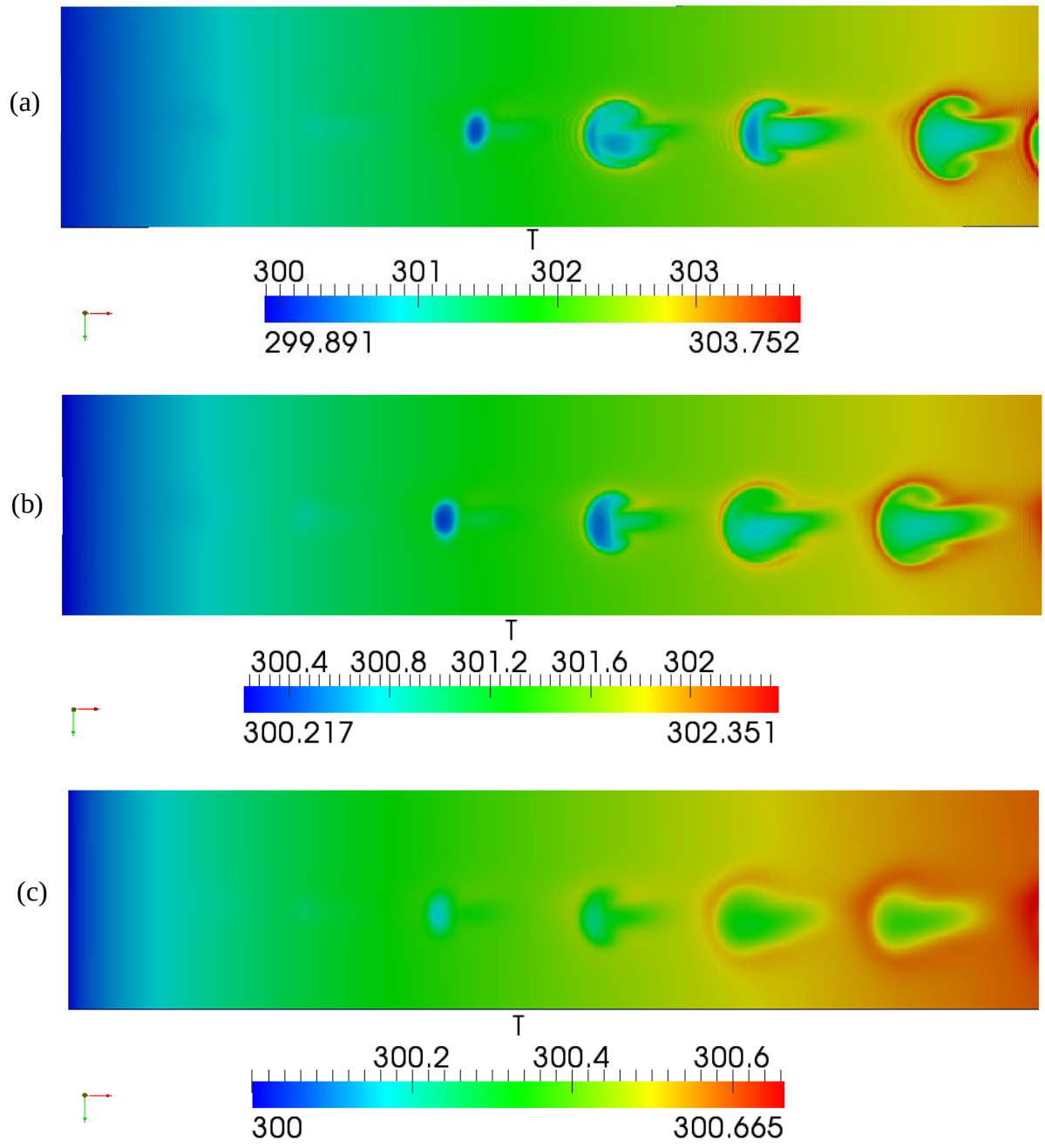

Figure 42. Temperature field on the surface at different Prandtl numbers: (a) Pr = 7 (b) Pr = 2 (c) Pr = 0.2.

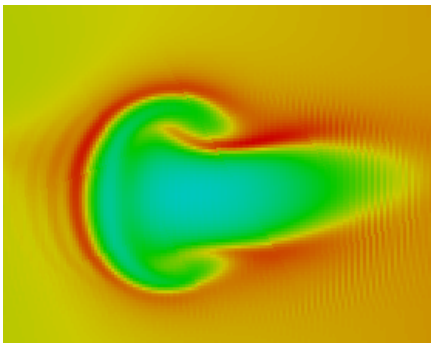

Figure 43. Numerical oscillation in the case of Pr = 7.

4.3.5.2 Numerical scheme

The simulations above use fourth order scheme in space and second order scheme in time. They show much better "resolution" than the simulations with second order scheme in space and first order in time, especially for the temperature field.

Figure 44 shows that the temperature field of the case using second order scheme for Pr = 2 (b) is much more blurred than the case using fourth order scheme (a). Even a rise of Prandtl number in Figure 42 (c) cannot help to increase the "resolution".

The reason of the blurry temperature fields of second order cases is large artificial diffusivity in the nature of second order numerical scheme. The artificial diffusivity is not physical, but works in a similar way to make the temperature field blurred as the physical thermal diffusivity. So low order numerical scheme cannot be used to resolve field with high gradient, even with low physical diffusivity and high mesh resolution.

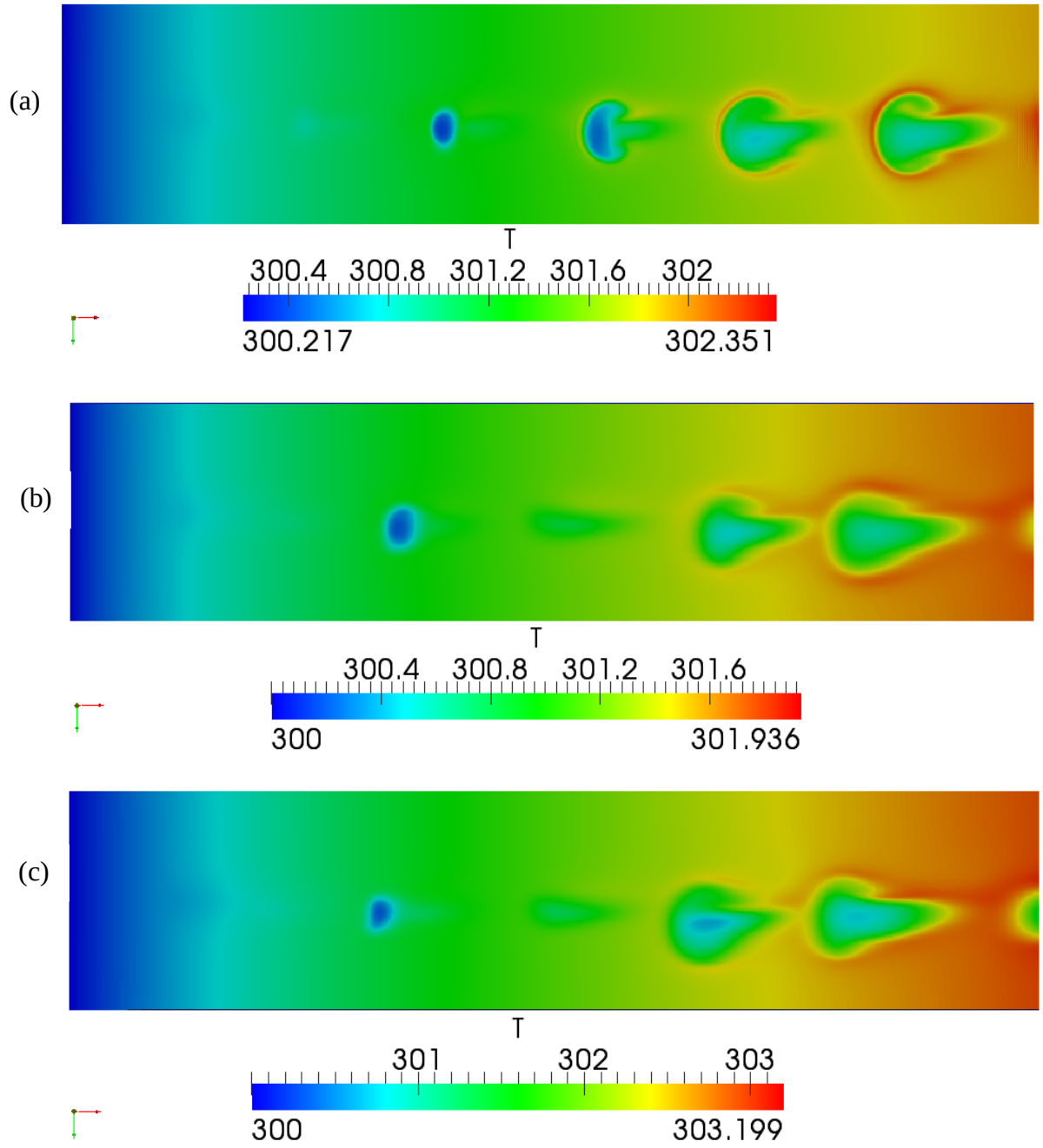

Figure 44. Temperature field on the surface for different orders of numerical scheme and Prandtl numbers: (a) fourth order, Pr = 2 (b) second order, Pr =2 (c) second order, Pr = 7.

5. CONCLUSION

A turbulent wake is generated when fluid flows past a sphere in the water. The wake will spread and interact with the surface and produce phenomena like surface roughness, wave motion and surface temperature change. The surface of ocean is often found to be colder or warmer than the water just a few millimeters below. Therefore, the wake of an underwater object can result in a thermal signature on the ocean surface by transporting the fluid from below to the surface.

This work focus on the direct numerical simulation on flow past a sphere at moderate Reynolds numbers, such as Re= 300 and 500. The simulation is performed by OpenFOAM, an open-sourced code for Computational Fluid Dynamics (CFD). According to the numerical results, periodic vortex shedding happens at Re = 300 and 500. The thermal surface signature can be visualized by performing constant heat flux into the surface at Re = 500.

The surface signatures are periodic and contain pairs of vortices with opposite direction of rotation. The velocity profile behind the sphere results in a cylindrical vortex sheet, which is reorganized into vortex rings due to complex instability effects. The vortex rings attaches the surface and form the pairs of vortices with opposite direction of rotation in the surface signatures. The phenomenon of surface divergence and convergence takes place in the center and on the edge of the surface signatures respectively.

The future work can explore the effect of surface deformation and buoyancy to the result. And flow past a sphere at higher Reynolds numbers should be simulated using turbulence models because the Reynolds numbers of flow past an underwater object are usually very high in the nature.

REFERENCES

[1] Achenbach, E. 1974. Vortex shedding from spheres. *Journal of Fluid Mechanics*, 62 (02), pp. 209--221.

[2] Batchelor, G. 1973. *An introduction to fluid dynamics*. Cambridge, UK: University Press.

[3] Behind Blue Lines. 2009. *What is State of the Art in Submarine Detection? - Behind Blue Lines*. [online] Available at: http://www.behindbluelines.com/2009/07/22/what-is-state-of-the-art-in-submarine-detection/ [Accessed: 3 Apr 2014].

[4] Bernal, L. and Kwon, J. 1989. Vortex ring dynamics at a free surface. *Physics of Fluids A: Fluid Dynamics (1989-1993)*, 1 (3), pp. 449--451.

[5] Bernal, L., Hirsa, A., Kwon, J. and Willmarth, W. 1989. On the interaction of vortex rings and pairs with a free surface for varying amounts of surface active agent. *Physics of Fluids A: Fluid Dynamics (1989-1993)*, 1 (12), pp. 2001--2004.

[6] Brocchini, M. and Peregrine, D. 2001. The dynamics of strong turbulence at free surfaces. Part 1. Description. *Journal of Fluid Mechanics*, 449 pp. 225--254.

[7] Dallmann, U., Gebing, H. and Vollmers, H. 1993. *Bluff-body wakes, dynamics and instabilities*. Berlin: Springer-Verlag.

[8] Guschin, V., Kostramov, A., Matyushin, P. and Pavlyukova, E. 2001. Direct numerical simulation of the transitional separated fluid flows around a sphere. *Computational Fluid Dynamics Journal*, 10 (3), pp. 344--349.

[9] Issa, R. I. 1986. Solution of the implicitly discretised fluid flow equations by operator-splitting. *Journal of Computational Physics*, 62 (1), pp. 40--65.

[10] Jasak, H. 1996. Error analysis and estimation for the finite volume method with applications to fluid flows. PhD thesis. Imperial College, University of London.

[11] Johnson, T. and Patel, V. 1999. Flow past a sphere up to a Reynolds number of 300. *Journal of Fluid Mechanics*, 378 pp. 19--70.

[12] Jones, D. and Clarke, D. 2008. Simulation of the Flow Past a Sphere using the Fluent Code. Fishermans Bend, Victoria, Australia: Maritime Platforms Division, DSTO Defence Science and Technology Organisation.

[13] Kim, H. and Durbin, P. 1988. Observations of the frequencies in a sphere wake and of drag increase by acoustic excitation. *Physics of Fluids (1958-1988)*, 31 (11), pp. 3260--3265.

[14] Lamb, H. 1945. *Hydrodynamics*. New York: Dover publications.

[15] Magarvey, R. and Bishop, R. L. 1961. Transition ranges for three-dimensional wakes. *Canadian Journal of Physics*, 39 (10), pp. 1418--1422.

[16] Melville, W. 1996. The role of surface-wave breaking in air-sea interaction. *Annual Review of Fluid Mechanics*, 28 (1), pp. 279--321.

[17] Mittal, R. 1999. Planar symmetry in the unsteady wake of a sphere. *AIAA Journal*, 37 (3), pp. 388--390.

[18] Nakamura, I. 2008. Steady wake behind a sphere. *Physics of Fluids (1958-1988)*, 19 (1), pp. 5--8.

[19] Natarajan, R. and Acrivos, A. 1993. The instability of the steady flow past spheres and disks. *Journal of Fluid Mechanics*, 254 pp. 323--344.

[20] Patankar, S. V. and Spalding, D. B. 1972. A calculation procedure for heat, mass and momentum transfer in three-dimensional parabolic flows. *International Journal of Heat and Mass Transfer*, 15 (10), pp. 1787--1806.

[21] Paulson, C. and Simpson, J. 1981. The temperature difference across the cool skin of the ocean. *Journal of Geophysical Research: Oceans (1978--2012)*, 86 (C11), pp. 11044--11054.

[22] Pedlosky, J. 1979. *Geophysical Fluid Dynamics*. New York: Springer Verlag.

[23] Peltzer, R. D. 1984. *Remote Sensing of the USNS Hayes Wake*. Washington, D.C.: Naval Research Laoratory.

[24] Peric, M. 1985. A finite volume method for the prediction of three-dimensional fluid flow in complex ducts. PhD thesis. Imperial College, University of London.

[25] Ploumhans, P., Winckelmans, G., Salmon, J. K., Leonard, A. and Warren, M. 2002. Vortex Methods for Direct Numerical Simulation of Three-Dimensional Bluff Body Flows: Application to the Sphere at Re = 300, 500, and 1000. *Journal of Computational Physics*, 178 (2), pp. 427--463.

[26] Rhie, C. and Chow, W. 1983. Numerical study of the turbulent flow past an airfoil with trailing edge separation. *AIAA Journal*, 21 (11), pp. 1525--1532.

[27] Roos, F. W. and Willmarth, W. W. 1971. Some experimental results on sphere and disk drag. *AIAA Journal*, 9 (2), pp. 285--291.

[28] Sakamoto, H. and Haniu, H. 1990. A study on vortex shedding from spheres in a uniform flow. *Journal of Fluids Engineering*, 112 (4), pp. 386--392.

[29] Taneda, S. 1956. Experimental investigation of the wake behind a sphere at low Reynolds numbers. *Journal of the Physical Society of Japan*, 11 (10), pp. 1104--1108.

[30] Taneda, S. 1978. Visual observations of the flow past a sphere at Reynolds numbers between 104 and 106. *Journal of Fluid Mechanics*, 85 (01), pp. 187--192.

[31] Tomboulides, A. G. and Orszag, S. A. 2000. Numerical investigation of transitional and weak turbulent flow past a sphere. *Journal of Fluid Mechanics*, 416 pp. 45--73.

[32] Tomboulides, A. G., Orszag, S. and Karniadakis, G. E. 1993. Direct and large eddy simulations of axisymmetric wakes. *AIAA paper*, 546.

[33] Wu, J. and Faeth, G. 1993. Sphere wakes in still surroundings at intermediate Reynolds numbers. *AIAA Journal*, 31 (8), pp. 1448--1455.